

AKARI Infrared Camera Observations of the 3.3 μm PAH Feature in *Swift*/BAT AGNs

Angel CASTRO¹, Takamitsu MIYAJI^{1,2}, Mai SHIRAHATA^{3,4}, Kohei ICHIKAWA⁵, Shinki OYABU⁶,
David M. CLARK¹, Masatoshi IMANISHI⁷, Takao NAKAGAWA⁴, Yoshihiro UEDA⁵

¹*Instituto de Astronomía, Universidad Nacional Autónoma de México (UNAM), Ensenada, Baja California, México*

(mailing address: PO Box 439027, San Diego, CA 92143-9027, USA)

²*University of California, San Diego, Center for Astrophysics and Space Sciences, 9500 Gilman Drive, La Jolla, CA 92093-0424, USA*

³*National Astronomical Observatory of Japan (NAOJ), 2-21-1 Osawa, Mitaka, Tokyo 181-8588, Japan*

⁴*Institute of Space and Astronautical Science (ISAS), Japan Aerospace Exploration Agency (JAXA), 3-1-1 Yoshino-dai, Chuo-ku, Sagamihara 252-5210*

⁵*Department of Astronomy, Kyoto University, Kitashirakawa-Oiwake-cho, Sakyo-ku, Kyoto 606-8502*

⁶*Graduate School of Science, Nagoya University, Furo-cho, Chikusa-ku, Nagoya, Aichi 464-8602, Japan*

⁷*Subaru Telescope, 650 North Aohoku Place, Hilo, Hawaii, 96720, USA*
acastro@astrosen.unam.mx

(Received ; accepted)

Abstract

We explore the relationships between the 3.3 μm polycyclic aromatic hydrocarbon (PAH) feature and active galactic nucleus (AGN) properties of a sample of 54 hard X-ray selected bright AGNs, including both Seyfert 1 and Seyfert 2 type objects, using the InfraRed Camera (IRC) on board the infrared astronomical satellite *AKARI*. The sample is selected from the 9-month *Swift*/BAT survey in the 14–195 keV band and all of them have measured X-ray spectra at $E \lesssim 10$ keV. These X-ray spectra provide measurements of the neutral hydrogen column density (N_{H}) towards the AGNs. We use the 3.3 μm PAH luminosity ($L_{3.3\mu\text{m}}$) as a proxy for star formation activity and hard X-ray luminosity ($L_{14-195\text{keV}}$) as an indicator of the AGN activity. We search for possible difference of star-formation activity between type 1 (un-absorbed) and type 2 (absorbed) AGNs. We have made several statistical analyses taking the upper-limits of the PAH lines into account utilizing survival analysis methods. The results of our $\log(L_{14-195\text{keV}})$ versus $\log(L_{3.3\mu\text{m}})$ regression shows a positive correlation and the slope for the type 1/unobscured AGNs is steeper than that of type 2/obscured AGNs

at a 3σ level. Also our analysis show that the circum-nuclear star-formation is more enhanced in type 2/absorbed AGNs than type 1/un-absorbed AGNs for low X-ray luminosity/low Eddington ratio AGNs, while there is no significant dependence of star-formation activities on the AGN type in the high X-ray luminosities/Eddington ratios.

Key words: galaxies: active — galaxies: Seyfert — X-rays: galaxies

1. Introduction

A fundamental question on the accretion onto supermassive black holes (SMBHs) at the centers of galaxies is the fueling mechanism, where gas is accreted from a kilo-parsec scale to a sub-parsec scale towards the black hole (BH; e.g. Alexander & Hickox 2012; for review). Some of the important mechanisms that can be responsible for this process are wind from the circum-nuclear star formation region (e.g. Umemura 1997; Ohsuga & Umemura 2001; Kawakatu & Wada 2008), tidal triggering by a companion galaxy (Noguchi 1988; for review) or a minor merger with a satellite galaxy (Gaskell 1985; Mihos & Hernquist 1994; Taniguchi 1997). On the other hand, it is also suggested that once AGNs are ignited, feedback from AGNs may clear surroundings from cold gas and quench star formation (e.g. Bundy et al. 2008; Lagos et al. 2008). In this context, investigating star formation activity in various types of AGNs is relevant in order to give observational clues to these scenarios.

There are some lines of observational evidence that the simplest version of unified theory of active galactic nuclei (AGNs), which postulates that difference between type 1 and type 2 AGNs are solely the viewing angle effect (e.g. Antonucci 1993; Urry & Padovani 1995), needs modifications. It has long been recognized that the fraction of absorbed (type 2) AGNs decrease with luminosity (Lawrence & Elvis 1982; Ueda et al. 2003; La Franca et al. 2005; Shinozaki et al. 2006; Hasinger 2008; Ueda et al. 2014), although it might be because of the selection effect based on X-rays or optical emission lines (Lawrence & Elvis 2010). A similar trend has been observed in optical/IR (e.g. Maiolino & Risaliti 2007) and Ichikawa et al. (2012b) in the X-ray/IR. Simpson (2005) also found that the fraction of type 1 AGNs increases with luminosity and shows that the faint-end slope of the AGN luminosity function steepens considerably when a correction for the 'missing' type 2 is made.

Also, clustering studies indicate some systematic difference of large-scale environments between type-1 and type-2 AGNs (Cappelluti et al. 2010; Allevalo et al. 2011) (but see also Hickox et al. 2010 for results for absorbed and un-absorbed QSOs). These observations suggest that type 1 (unabsorbed) and type 2 (absorbed) AGNs have some systematic differences in their intrinsic properties, beyond the viewing angle effect, such as opening angle/distribution of the absorbing material (e.g. Ramos Almeida et al. 2011; Elitzur et al. 2012), and these two classes may be in different stages of AGN evolution, with a significant overlap. If a circum-nuclear

starburst plays a major role in feeding the central SMBH at the early stage of the AGN activity, where the absorbing torus may have a thicker geometry with a larger covering factor, it is more likely to be observed as a type 2 AGN.

The use of very hard X-ray ($E \gtrsim 10$ keV) surveys such as available with *Swift* Burst Alert Telescope (BAT), (Tueller et al. 2008; Tueller et al. 2010; Ajello et al. 2012) or *INTEGRAL* (Krivonos et al. 2010) allows us to select AGNs with a wide range of absorbing column densities, since photoelectric absorption is negligibly small. These very hard X-ray surveys provide an efficient way of constructing a clean and highly unbiased census of AGNs activities in the universe, which include those that are heavily obscured up to moderately Compton-thick column densities ($\log(N_{\text{H}})[\text{cm}^{-2}] \lesssim 25$). The *Swift*/BAT AGN catalog is one of the well-studied surveys including soft X-ray, optical, and infrared observations (e.g. Winter et al. 2009; Winter et al. 2010; Ichikawa et al. 2012a).

The polycyclic aromatic hydrocarbon (PAH) features have been used to disentangle between AGN and starbursts (SB) in Ultra-Luminous InfraRed Galaxies (ULIRGs; e.g. Sanders et al. 1988; Lutz 1998), since observationally these features have been found to be weak or absent in classical AGNs but generally strong in starbursts (Moorwood 1986; Genzel et al. 1998; Imanishi & Dudley 2000). The PAH emission act as an indicator for the presence of pumping far-ultraviolet (FUV) photons and reveals the presence of massive stars (Genzel et al. 1998; Tielens 2008). The source of the UV radiation is generally considered to be from the massive stars in the star-formation region rather than AGNs, because in AGNs, X-ray photons destroy the PAH molecules (Voit 1992). Thus generally PAH emission features seen in the infrared spectra at, e.g. $3.3 \mu\text{m}$, $6.2 \mu\text{m}$, $7.7 \mu\text{m}$, $8.6 \mu\text{m}$, and $11.2 \mu\text{m}$, may be used as an indicator of star-formation activity with little contamination from AGNs, and thus provides a tool for investigating star formation activities in AGNs.

PAH molecules could be excited by UV photons from AGNs in some circumstances without being destroyed. However, such circumstances are limited. For example, Howell et al. (2007) measured bright PAH knots directly along the ionization cone of the Seyfert 2 galaxy NGC 1068. Even in that case, it was not clear whether the AGN radiation can directly enhance the PAH emission or it is a result of stimulating the formation of OB stars and UV photons from these excite PAHs.

There have been a number of studies that have investigated the PAH emission in a sample of known AGNs and investigated the differences in PAH emission properties among various types of AGNs. Clavel et al. (2000) and Freudling et al. (2003) showed that weak PAH and hot dust are more associated with type 1 AGNs while cooler dust and strong PAHs with type 2 AGNs. Haas et al. (2010) argued that nuclear starburst should be weaker in low-luminosity AGNs. Studying the stellar population of the central ~ 200 pc of a sample of 79 nearby galaxies, most of them Seyfert 2s, Cid Fernandes et al. (2004) found no correlation between the star formation in the nucleus, neither for the host morphology nor for the presence

of companions. The star formation history deduced from their study varied significantly among Seyfert 2s.

Imanishi (2003) and Imanishi & Wada (2004) investigated the relation between nuclear SB and AGN activities in a sample of 32 Seyfert 2 galaxies and 23 Seyfert 1 galaxies using ground-based spectroscopy. They found that SB correlates with nuclear activity. However, they found no significant difference between type 1 sources and type 2 sources. Similar studies by Watabe et al. (2008) and by Oi et al. (2010) found no significant difference of star-formation between type 1 and type 2 Seyferts either.

Diamond-Stanic & Reike (2012) measured the AGN luminosity of a sample of Seyfert galaxies using the $[\text{O IV}]\lambda 25.89 \mu\text{m}$ emission line and the star-forming luminosity using the $11.3 \mu\text{m}$ aromatic feature. They found strong correlation in the relationship between nuclear star formation ratio (SFR) (measured on $r = 1 \text{ kpc}$ scales) and the BH accretion rate but only weakly correlated with extended ($r > 1 \text{ kpc}$) star formation in the host galaxy. Their results do not exhibit any statistically significant differences between type 1 and type 2 Seyfert objects.

In order to investigate the least possible biased AGN sample, we have performed 2.5–5 μm infrared spectroscopy of hard X-ray selected AGNs from the 9-month catalog (Tueller et al. 2008) of the *Swift*/BAT survey with the grism mode of the InfraRed Camera (IRC) instrument on board the Japanese space infrared observatory *AKARI*. The sample contains AGNs with a wide range of N_{H} , including both highly obscured AGNs and unobscured AGNs. In this work, we use the 3.3 μm PAH emission detected in our spectral range as a proxy for the star formation activity to explore the link between AGN activity, column densities towards the nucleus, AGN type and star formation.

This paper is organized as follows. In section 2 we explain our sample selection criteria. In section 3, we describe the *AKARI*/IRC observation. The data reduction of the IRC spectra and the subsequent measurements of the 3.3 μm PAH flux are explained in section 4. In section 5 the regression analysis and statistical tests employed are described. Results of the research are shown in section 6. Discussion and conclusions follows in sections 7 and 8, respectively. Throughout this paper, luminosities are calculated using $H_0 = 75 \text{ km s}^{-1} \text{ Mpc}^{-1}$, $\Omega_{\text{m}} = 0.3$ and $\Omega_{\Lambda} = 0.7$.

2. Sample Selection

In this work, we have selected our sample of AGNs from the 9-month *Swift*/BAT catalog (Tueller et al. 2008) for the *AKARI*/IRC spectroscopy. We have excluded blazars, where the X-ray emission is dominated by highly collimated beams towards us. Almost all of the AGNs have published measurements of detailed X-ray spectroscopy at $E \lesssim 10 \text{ [keV]}$ from *XMM-Newton*, *ASCA*, *Chandra*, *Beppo-SAX*, *Suzaku*, and *Swift* X-ray Telescopes (Winter et al. 2009; Ichikawa et al. 2012a). The most important quantity derived from the $E \lesssim 10 \text{ [keV]}$ X-ray spectroscopy is the absorbing column density of the neutral gas, expressed by the equivalent hydrogen column

density, N_{H} .

Thirty-two *Swift*/BAT AGNs are from our own observations made as a part of the “AGNUL” (AGN and ULIRG) group proposal for the *AKARI* Mission Program 3 (MP3), which covers the post-helium phase of the *AKARI* mission. In the first cycle of MP3, we have selected our objects among highly absorbed AGNs ($\log(N_{\text{H}}) > 23.5[\text{cm}^{-2}]$) and well-known bright AGNs. In the second cycle, we selected our targets such that the sample is spread over all $\log(N_{\text{H}})$ levels. The remaining 22 have been observed by other groups and we obtained the data from public archives. The archival data that we have used for our analysis were from observations with the same instrumental configuration. We intended to obtain spectra of almost all remaining non-blazar AGNs in the 9-month *Swift*/BAT catalog during the third cycle of the MP3 program. However, it became impossible due to the unfortunate failure of the mechanical cryogenic cooler on board *AKARI*, which happened in the winter of 2010. While obtaining spectra for all the AGNs in a complete sample is desirable, the selection criteria of our current sample are mainly based on the X-ray absorption (first cycle) and visibility considerations (both cycles), rather than the far infrared properties or any star-formation indicator. Also the abstracts of the proposals of the observers of the archival data show that they did not select based on star-formation indicators. This is in contrast with other studies that use ULIRGS/LIRGS. Thus our sample enables us to probe the star formation in AGNs in an unbiased manner.

In our sample (see table 1), 26 AGNs are optical type 1 AGNs (Seyfert optical type ≤ 1.5) and 28 type 2 AGNs (Seyfert optical type > 1.5). Our selected sample also has detailed X-ray spectra from the *XMM-Newton*, *Chandra*, *ASCA*, *Suzaku*, and *SWIFT*/XRT in $0.3 \lesssim E[\text{keV}] \lesssim 12$ (Winter et al. 2009; Ichikawa et al. 2012a). The distribution of $\log(L_{14-195 \text{ keV}})$ for the overall sample is shown in figure 1(a). For all objects in our sample X-ray-derived neutral hydrogen column densities were obtained from these spectra. Figure 1(b) shows the N_{H} distribution of the sample. In the cases where N_{H} value is not explicitly provided by Winter et al. (2009) (in those cases where the original X-ray spectra were well fit by a simple absorbed power law model and thus, consistent with a un-absorbed AGN) we took the N_{H} value from Ichikawa et al. (2012a).

3. Observations

Infrared 2.5–5 μm spectroscopy of our hard X-ray selected AGNs was performed with the IRC spectrograph (Onaka et al. 2009) on board the *AKARI* Infrared satellite (Murakami et al. 2007) during the Phase 3-mission program. The NIR channel of IRC has two dispersion spectroscopic elements, NP (low resolution prism) and NG (high resolution grism). The spectroscopic observations can be made with or without a slit.

For our observations, the high resolution grism (NG) were used. Among the three slit/window sizes available, the $1' \times 1'$ square window was used for all of our observations. This window size is optimized for the spectroscopy of the point sources, where the size was

determined such that the aperture is larger than the absolute pointing accuracy of the satellite ($\lesssim 30''$). This configuration is designated as b; Np (NG for point sources; Onaka et al. 2009). The spectral resolution of the NG is $R = \lambda/\delta\lambda = 120$ at $\lambda = 3.6 \mu\text{m}$ (Ohyama et al. 2007) for point sources. The Astronomical Observation template (AOT) of our observations was IRCZ4, where, during an orbit of observation on target, 4 spectroscopic exposures are made with the grism, followed by a reference imaging exposure without a disperser, and 4 additional exposures with the grism. Five dark frames are taken before and after the observations of the target.

With the increased number of hot pixels during the phase 3 period, we followed the recommendation to make redundant observations with at least 3 orbits for one target. Thus, for those objects we proposed, we attempted to make 3 or 5 orbits of observation on each. However, not all requested observations were finally achieved and some objects have only one or two orbits of observations. The log of observations is shown in table 1.

4. Data Reduction and Analysis

4.1. Reduction

The spectra have been reduced using the IDL package, “IRC Spectroscopy Toolkit for Phase 3 data Version 20110301” (Ohyama et al. 2007)¹ (hereafter referred to as “the toolkit”). The toolkit performs the basic reduction pipeline of linearity correction, background and dark subtraction and the division by flat frames of the two-dimensional (2D) spectra (Onaka et al. 2009). During the pipeline processing, the toolkit removes the hot and bad pixels upon coadding individual images and/or upon correcting the image by its own dark image. For the NG grism, the 2D spectra corresponds to $d\lambda = 0.0097 \mu\text{m}/\text{pix}$ along the dispersion and the $1''.46/\text{pix}$ perpendicular to it (Ohyama et al. 2007). We adopted a narrow aperture of 3 pixels ($\text{nsum}=3$; $4''.38$), corresponding to the typical full-width of the image PSF for achieving the best S/N in creating the 1-dimensional (1D) spectra. For some cases small shifts of the aperture position on the sky were required. The 1D spectra from different orbits of an object have been averaged to obtain the final spectrum. The calibration uncertainties of *AKARI*/IRC spectra become large when $\lambda_{\text{obs}} > 4.8 \mu\text{m}$. We arbitrarily excluded the $\lambda_{\text{obs}} < 2.55 \mu\text{m}$ and $\lambda_{\text{obs}} > 4.85 \mu\text{m}$ edges in order to avoid bad S/N data. Resultant spectra in the rest-frame wavelength ($\lambda_{\text{rest}} = \lambda_{\text{obs}}/(1+z)$) are shown in figure 2. The aperture size corresponds to ~ 2 kpc at the distance of ~ 100 Mpc and thus our spectra are collected from regions weighted towards the central bulge-sized region around the nucleus and the contributions of disks are relatively suppressed.

¹ <http://www.ir.isas.jaxa.jp/ASTRO-F/Observation/>

4.2. Correction for Galactic Extinction

Before proceeding further, we have corrected our 2.5–5 μm spectra for Galactic extinctions as follows. Galactic extinctions in the K -band at 2.2 μm (A_K) were taken from the NED ExtraGalactic Catalog. Extinction values agree with Schlegel et al. (1998) infrared-based dust map from the COBE/DIRBE and IRAS/ISSA which assumes a Cardelli et al. (1989) extinction law. Nishiyama et al. (2006) determined the ratios of total to selective extinction in the IRSF/SIRIUS near-infrared (J,H,K_S) and established that the extinction in the 2–3 μm wavelength range is well fitted by a power-law with a steep decrease $A_\lambda \propto \lambda^{-2}$ toward the Galactic centre. We have made a small correction from A_K to A_{K_S} ($\lambda_{\text{eff}} = 2.14 \mu\text{m}$) using this relation. Then, we apply the adopted extinction law and the relation A_λ/A_{K_S} (Román-Zúñiga et al. 2007; Nishiyama et al. 2009) in order to do the flux correction considering the proper line-of-sight Galactic extinctions to the studied AGNs across the whole 2.5–5 μm range.

4.3. The PAH Line Strength Measurements

The software package MINUIT (James & Roos 1975) has been used to obtain the fitted parameter values and errors for the following analysis. By assuming a single Gaussian component for the 3.3 μm PAH emission feature we determined the peak, the central wavelength and the dispersion σ of the line profile based on the χ^2 minimization over a local continuum. The line flux is the integration over the Gaussian profile.

We have modeled the continuum in the rest-frame wavelength range between 3.15 and 3.35 μm with a power-law, if no notable feature exists near 3.3 μm . In some cases, there are nearby features such as the 3.1 μm H₂O ice covered dust and the PAH 3.4 μm sub-peak. In these cases, we have included these features in the fitting process. In all cases with apparent PAH 3.3 μm emission feature, we see the 3.1 μm absorption. In some cases, we see the PAH 3.4 μm sub-peak. In order to determine the 3.3 μm feature parameters, we fit the rest-frame $2.75 < \lambda[\mu\text{m}] < 3.85$ spectrum $[f_{\text{rest}}(\lambda)]$ with the form:

$$\begin{aligned}
 f_{\text{rest}}(\lambda) = & A_{\text{PL}} \lambda^{-\Gamma} e^{-\tau_{3.1} \text{gauss}(\lambda - \lambda_{3.1}, \sigma_{3.1})} \\
 & + f_{3.3} \text{gauss}(\lambda - \lambda_{3.3}, \sigma_{3.3}) \\
 & + f_{3.4} \text{gauss}(\lambda - \lambda_{3.4}, \sigma_{3.4}).
 \end{aligned} \tag{1}$$

The fitting parameters are A_{PL} , Γ , τ_X, f_X, λ_X and σ_X , where the subscript X (3.1, 3.3 or 3.4) represents the nominal wavelength (in μm) of the feature. The first term represents the underlying power-law continuum with normalization A_{PL} and index Γ , multiplied by the 3.1 μm ice covered dust absorption feature with an effective optical depth $\tau_{3.1 \mu\text{m}}$. The second and third terms represent the PAH 3.3 μm emission feature and the 3.4 μm sub-peak respectively with line fluxes f_X and width σ_X . The function $\text{gauss}(\lambda, \sigma) = 1/(\sqrt{2\pi}\sigma) \exp(-\lambda^2/2\sigma^2)$ is the Gaussian function normalized to unity. The central wavelengths are allowed to vary slightly

near the nominal wavelength of each feature during the fit. The third term (the 3.4 μm PAH emission sub-peak) is included in the fit if the sub-peak is clearly visible.

From the subsample of detected 3.3 μm PAH emission features Gaussian $\sigma_{3.3}$ parameter was found to range from 0.025 μm to 0.04 μm , with an average value of 0.030 μm . For those objects for which the PAH 3.3 μm is not visible or only marginally visible, we fixed the parameters $\lambda_{3.3}$ and $\sigma_{3.3}$ to 3.28 and 0.030 μm respectively and investigated the variation of χ^2 as a function of $f_{3.3} \geq 0$. If the minimum χ^2 (best-fit case) is smaller than 2.7 below the χ^2 value at $f_{3.3} = 0$, we consider the line detected and report the best-fit $f_{3.3}$, otherwise, we consider it a non-detection and report the 90% upper limit to $f_{3.3}$ corresponding to $\Delta\chi^2 = 2.7$ from the best-fit value.

All fitted fluxes and luminosities of the 3.3 μm PAH emission lines of the AGNs from our X-ray AGN selected sample are summarized in table 2. For the PAH fluxes, 1σ errors are reported for detections and the 90% upper limits are reported for non-detections. We have converted our 3.3 μm flux to the line luminosity. The histogram of $\log(L_{3.3\mu\text{m}})$ is shown in figure 3(a), where upper limits are indicated. The values of $\log(L_{3.3\mu\text{m}})$ and $\log(L_{14-195\text{keV}})$ are plotted as a function of luminosity distance in figure 3(b).

5. The Regression Analysis and Statistical Tests

The analysis of IRC spectra of our sample have both detections and non-detections of the PAH 3.3 μm feature. In this case, usual statistical techniques are no longer applicable. To study data containing both detections and non-detections, we apply a series of survival analysis methods to the data using the ASURV package (Feigelson & Nelson 1985; Isobe et al. 1986; Lavalley et al. 1992) to account for upper-limits (left censorship) of the 3.3 μm line luminosity. In table 3 we explored the correlation between as well as the correlation between the luminosities normalized by the black hole mass (M_{BH}). Masses presented in this work were collected from the literature where mass is derived from the 2MASS K -band stellar magnitudes (Mushotzky et al. 2008; Vasudevan et al. 2009; Winter et al. 2009).

Because of the presence of a scaling relation between the M_{BH} and the stellar mass of the bulge, the variable $L_{3.3\mu\text{m}}/M_{\text{BH}}$ can be considered a proxy for specific star formation rate (SSFR). The variable $L_{14-195\text{keV}}/M_{\text{BH}}$ is a proxy to Eddington ratio (λ_{edd}). To test the difference of star formation activities between different types of AGNs the following correlation analysis have been made. First, based on Tueller et al. (2008) optical classification, we divide our sample into two sub samples of optical type 1 AGNs and optical type 2 AGNs. Second, we repeated the analysis but in a column density classification scheme. We called X-ray type 1 AGNs the objects with $N_{\text{H}} \leq 10^{22} \text{ cm}^{-2}$ and X-ray type 2 those objects with $N_{\text{H}} > 10^{22} \text{ cm}^{-2}$.

In order to explore a possible correlation between the two variables the Cox regression method (where only the dependent variable have censored data) was employed. The parametric E-M (estimate and maximize) algorithm was used to determine the slope coefficients in a linear

regression model. This method is a general approach to the problem of finding maximum likelihood estimates for censored data sets (Isobe et al. 1986) assuming a normal distribution of residuals. If censored data are not present this method yields the usual least-square results.

To test the hypothesis that $L_{3.3\mu\text{m}}/M_{\text{BH}}$ for Seyfert 1 and Seyfert 2 objects have the same distribution, the Gehan’s extension of the Wilcoxon test, logrank test and Peto-Peto tests were used. We report the survival analysis probabilities, P, from the mentioned tests in table 4. It shows that the probability that the distribution of 3.3 μm PAH luminosities of Seyfert 1 and Seyfert 2 objects from our sample to be the same. A P value ≤ 0.05 means that the two-subsamples differ at a statistically significant level, otherwise they are consistent with belonging to the same parent population (LaMassa et al. 2012). Similar analysis was carried out for non- M_{BH} normalized data (see table 4). The Kaplan-Meier estimator was used to obtain mean values for each sub-sample with the TWOST application under ASURV. These tests are made for sub-samples divided by $L_{14-195\text{keV}}/M_{\text{BH}}$ and $L_{14-195\text{keV}}$ for the tests for $L_{3.3\mu\text{m}}/M_{\text{BH}}$ and $L_{3.3\mu\text{m}}$ respectively.

For the type 1 vs type 2 comparisons of $L_{3.3\mu\text{m}}$ of the low $L_{14-195\text{keV}}$ (Low – L_{X}) and high $L_{14-195\text{keV}}$ (High – L_{X}) samples, we further verify the statistical significance of the comparisons using the Bootstrap resampling method. We generate N_{boot} bootstrapped samples from each of the high and low $L_{14-195\text{keV}}$ samples. Each such bootstrapped sample contains the same number of objects (n_{obj}) as the original sample and each object in the bootstrapped sample is a random selection from the original sample, in which an object in the original may be selected in duplicate. The distribution of a statistical measure (e.g. mean value) from the N_{boot} redrawn samples is a good approximation of that from samples (each with a size of n_{obj}) randomly drawn from the underlying population. For each redrawn sample, we run the TWOST application, which gives the mean $\langle \log L_{3.3\mu\text{m}} \rangle$ for each of the type 1 and type 2 AGNs. Since our interest is to see whether there is any systematic difference between type 1 and type 2 AGNs, we make a histogram of the difference $\langle \log L_{3.3\mu\text{m}} \rangle_{\text{Sy1}} - \langle \log L_{3.3\mu\text{m}} \rangle_{\text{Sy2}}$ from the $N_{\text{boot}} = 600$ bootstrapped samples to verify the significance of the difference.

Since one of the major advantages of our sample is to have X-ray based N_{H} measurements for all AGNs, we can further explore the correlation using the N_{H} values rather the type 1/type 2 dichotomy. Thus we also investigate the correlation of $L_{3.3\mu\text{m}}/M_{\text{BH}}$ and $L_{3.3\mu\text{m}}$ with N_{H} . These tests should measure the “type” or “absorption” dependence of SFR/SSFR without making somewhat arbitrary decisions about type 1/type 2 borders.

6. Results

The results of our series of linear regression analyses using the E-M method are expressed through the generic expression $\log(A_i) = a_i \{ \log(B_i) - c_i \} + b_i$, where A_i is the independent variable, B_i is the dependent variable, a_i is the slope of the curve, b_i is the abscissa intersection point, and c_i is the average value of the corresponding independent variable of the given

relationship. The origin point of the distribution has been shifted to the average value of the independent variable in order to minimize the artificial correlation of errors of the a_i and b_i parameters. This is needed because ASURV does not provide the covariance matrix of parameter errors. We have studied the dependencies between the luminosity of the PAH at $\lambda_{\text{rest}} = 3.3 \mu\text{m}$ ($L_{3.3\mu\text{m}}$) emission line to the X-ray luminosity in the 14–195 keV band ($L_{14-195\text{keV}}$; also referred to as L_X):

$$\log(L_{3.3\mu\text{m}}) = a_0 \{ \log(L_{14-195\text{keV}}) - c_0 \} + b_0 \quad (2)$$

Likewise, we express the relationship between the black-hole mass normalized luminosities:

$$\log(L_{3.3\mu\text{m}}/M_{\text{BH}}) = a_1 \{ \log(L_{14-195\text{keV}}/M_{\text{BH}}) - c_1 \} + b_1. \quad (3)$$

A similar procedure was performed to explore a possible relationship between N_H and $L_{3.3\mu\text{m}}$ ($L_{3.3\mu\text{m}}/M_{\text{BH}}$):

$$\log(L_{3.3\mu\text{m}}) = a_2 \{ \log(N_H) - c_2 \} + b_2. \quad (4)$$

$$\log(L_{3.3\mu\text{m}}/M_{\text{BH}}) = a_3 \{ \log(N_H) - c_3 \} + b_3. \quad (5)$$

The regressions have been made for all AGNs in our sample as well as for $L_{14-195\text{keV}}$ and $L_{14-195\text{keV}}/M_{\text{BH}}$ -divided sub-samples for equation 4 and equation 5 respectively. The best-fit values and 1σ errors for each equation coefficient are given by the ASURV package and summarized in table 3 and the scatter diagram with the best-fit lines are shown in figure 4.

The average values of the independent variables used under this study are $c_0 = \langle \log L_{14-195\text{keV}} [\text{erg s}^{-1}] \rangle = 43.64$, $c_1 = \langle \log L_{14-195\text{keV}}/M_{\text{BH}} [\text{erg s}^{-1} M_{\odot}^{-1}] \rangle = 35.42$ and $c_2 = c_3 = \langle \log(N_H) [\text{cm}^{-2}] \rangle = 22.23$.

Based on our data analysis we do not find large discrepancy between the X-ray and optical classifications. Almost half of the sources, 26/54 (48%), have optical classifications of Sy 1-1.5. The mean X-ray column density for these objects corresponds to a low column density object (un-absorbed) with a $\log N_H = 20.83$. The 1.6-2.0 optically classified sources (28/54; 52%) have as expected a higher column density, $\log N_H = 23.35$. When we use the X-ray criteria the proportion is similar: 24 X-ray type 1 sources (44%) and 30 X-ray type 2 sources (56%).

We applied the generalized Cox's proportional hazard model to compute the correlation probabilities along with the E-M algorithm which calculates the linear regression coefficients. The results of the regressions are summarized in table 3.

As shown in table 3, the probabilities that a correlation is not present for the $\log(L_{14-195\text{keV}})$ versus $\log(L_{3.3\mu\text{m}})$ relationship is 0.01 and for $\log(L_{14-195\text{keV}}/M_{\text{BH}})$ versus $\log(L_{3.3\mu\text{m}}/M_{\text{BH}})$ is 0.002, implying that a correlation is present through the whole sample. We divided the sample according to the optical classification of the sources. The probability

that a correlation is not present for the optical Seyfert 1 objects is 0.02 for the $\log(L_{14-195\text{keV}})$ - $\log(L_{3.3\mu\text{m}})$ relationship and 0.005 for the M_{BH} normalized case, indicating significant correlations. For the optical Seyfert 2's, the probability that there is no correlation between $L_{14-195\text{keV}}$ and $L_{3.3\mu\text{m}}$ is 0.65, while the same probability is 0.1 between $\log(L_{14-195\text{keV}}/M_{\text{BH}})$ and $\log(L_{3.3\mu\text{m}}/M_{\text{BH}})$. Thus no significant correlation has been found between the AGN power and star-formation rate in Seyfert 2 galaxies. The correlation is marginal in the normalized case for Seyfert 2's.

The sample has been also subdivided according to a X-ray column density classification scheme instead of the optical classification. We call the sources with $N_{\text{H}} \leq 10^{22} \text{ cm}^{-2}$ ‘‘X-ray type 1 AGNs’’ and those with $N_{\text{H}} > 10^{22} \text{ cm}^{-2}$ ‘‘X-ray type 2 AGNs’’. The results in table 3 show that the difference between correlations in optical and X-ray AGN type division schemes are different by only about 4% from each other. Figure 4 shows the scatter diagrams between $\log(L_{14-195\text{keV}})$ and $\log(L_{3.3\mu\text{m}})$ as well as between $\log(L_{14-195\text{keV}}/M_{\text{BH}})$ and $\log(L_{3.3\mu\text{m}}/M_{\text{BH}})$. The best-fit regressions for the all-AGN sample as well as type-divided samples are shown. The error range of the regression line corresponding to $\Delta\chi^2 < 2.3$ (68% confidence for the two interesting parameters) is also shown as a shaded area in each panel for the all-AGN sample. In both figures, the regression line of type 1 AGNs shows a steeper slope than that of type 2 AGNs. The tendency is common for optically-divided types and X-ray divided types. The differences of the slopes between type 1 and type 2 regression curves are at the 2-3 σ levels.

To further verify this tendency, we have made further statistical tests. We divided the sample into high and low $L_{14-195\text{keV}}$ (or $L_{14-195\text{keV}}/M_{\text{BH}}$) and compared the mean $\log L_{3.3\mu\text{m}}$ (or $L_{3.3\mu\text{m}}/M_{\text{BH}}$) values of the type 1 and type 2 AGNs (see table 4) using a number of two-sample tests available in ASURV. We used the Gehan’s Generalized Wilcoxon test, logrank test and Peto & Peto Generalized Wilcoxon Test to determine the probability that the distributions of (S)SFR proxy among the type 1 and type 2 sub-samples are drawn from the same parent population separately for high and low $L_{14-195\text{keV}}$ (or $L_{14-195\text{keV}}/M_{\text{BH}}$) regimes. The only statistically significant difference between the type 1 and type 2 samples in these two-sample tests are in the $\langle \log(L_{3.3\mu\text{m}}) \rangle$ values of low X-ray luminosity sample. The difference is marginal in the M_{BH} normalized case.

The basic results of the regressions involving N_{H} (see equations (4) and (5)) are as follows. We do not find significant correlations between $\log(N_{\text{H}})$ and $\log L_{3.3\mu\text{m}}$ for the all-AGN sample (see figure 5(a)). However, if we divide the sample in two X-ray luminosity bins, a positive correlation has been observed in only low luminosity AGNs.

No significant correlation has been found between $\log(N_{\text{H}})$ and $\log(L_{3.3\mu\text{m}}/M_{\text{BH}})$ relationship in any of the all, high $\log(L_{3.3\mu\text{m}}/M_{\text{BH}})$ and low $\log(L_{3.3\mu\text{m}}/M_{\text{BH}})$ samples (see figure 5(b)).

On the right vertical axis of figure 4(a) the SFR, which is estimated by using the $L_{\text{FIR}} - L_{3.3\mu\text{m}}$ relation by Mouri et al. (1990) and the $L_{\text{FIR}} - \text{SFR}$ relation by Kennicutt (1998) using:

$$\log(SFR)[M_{\odot}\text{year}^{-1}] = \log(L_{3.3\mu\text{m}}[\text{erg s}^{-1}]) - 40.34 \quad (6)$$

On the upper horizontal axis of figure 4(b), approximate Eddington ratios $\lambda_{\text{Edd}} \equiv L_{\text{bol}}/L_{\text{Edd}}$ (see equation 7), where L_{bol} is the bolometric luminosity of the AGN and $L_{\text{Edd}} = 1.26 \times 10^{38} (M_{\text{BH}}/M_{\odot}) \text{erg s}^{-1}$ is the Eddington luminosity, corresponding to $L_{14-195\text{keV}}/M_{\text{BH}}$ values are indicated. The conversion has been made as follows. First, we convert from the 14–195 keV to unabsorbed 2–10 keV luminosity using an effective photon index of $\Gamma = 1.85$, which implies $L_{2-10\text{keV}}/L_{14-195\text{keV}} = 0.41$. This is based on Ueda et al. (2011), where average effective photon index between these two bands range from $\Gamma \approx 1.7$ at the low luminosity end to $\Gamma \approx 2.0$ in the low luminosity end. For the bolometric correction from 2–10 keV, we use $L_{\text{bol}}/L_{2-10\text{keV}} = 14$, from Lusso et al. (2012) for $\log(L_{2-10\text{keV}}) \approx 43.2$ type 1 AGNs, which is the average 2–10 keV unabsorbed luminosity of AGNs in our sample implied from the mean $\langle \log L_{14-195\text{keV}} \rangle$.

$$\lambda_{\text{Edd}} = L_{\text{Bol}}/L_{\text{Edd}} \sim 5 \times 10^{-38} (L_{14-195\text{keV}}[\text{erg s}^{-1}]/M_{\text{BH}}[M_{\odot}]) \quad (7)$$

The rough SSFR scale on the right axis of figure 4(b) is determined based on the combination of equation 6, the $M_{\text{BH}} - L_{K(\text{stellar})}$ relation from Mushotzky et al. (2008) and the stellar mass to K -band luminosity ratio, $M_{\text{stellar}}/L_{K(\text{stellar})} \sim 0.8$ (in solar units) (Brinchmann & Ellis 2000). The M_{BH} dependence of the ratio $M_{\text{BH}}/L_{K(\text{stellar})}$ is neglected and is evaluated at $\log(M_{\text{BH}}) = 8.27$, which is the mean value for our sample.

$$\log(SSFR)[\text{year}^{-1}] = \log(L_{3.3\mu\text{m}}[\text{erg s}^{-1}]) - \log(M_{\text{BH}}[M_{\odot}]) - 42.87 \quad (8)$$

Since there is significant scatter and luminosity/mass dependence in the conversions involved, these relations are only accurate to an order of magnitude.

The most significant result of our tests is the excess of $L_{3.3\mu\text{m}}$ of type 2/absorbed AGNs with respect to that of type 1/unabsorbed AGNs at low $L_{14-195\text{keV}}$ (Low – L_{X}). However, this excess is not observed at high $L_{14-195\text{keV}}$ (High – L_{X}). These results are worth scrutinizing and therefore we made bootstrap resampling to the each of the high and low $L_{14-195\text{keV}}$ samples as described in section 5. The bootstrap histograms of $\Delta_{12} \equiv \langle \log L_{3.3\mu\text{m}} \rangle_{\text{Sy1}} - \langle \log L_{3.3\mu\text{m}} \rangle_{\text{Sy2}}$ for 600 redrawn samples for each of the high and low $\log L_{14-195\text{keV}}$ sub-samples are shown in figure 6. In some redrawn samples where there are too many upper limits, the TWOST routine cannot determine the mean $\langle \log(L_{3.3\mu\text{m}}) \rangle_{\text{Sy1}}$ value and instead gives an NaN (not a number). There are 9/600 and 78/600 such for the high and low $L_{14-195\text{keV}}$ samples respectively. In these cases, we use the upper limit values to calculate the mean. The histograms of these cases are also overplotted in figure 6 under thick lines and indicated by symbols '<<<<<<'.</p>
</div>
<div data-bbox="87 773 885 900" data-label="Text">
<p>The bootstrap histogram shows that only 29 out of 600 bootstraps (5%) show $\langle \log L_{3.3\mu\text{m}} \rangle_{\text{Sy1}} - \langle \log L_{3.3\mu\text{m}} \rangle_{\text{Sy2}} > 0$ for the low $L_{14-195\text{keV}}$ sample, verifying the conclusion of the TWOST tests. This percentage is an overestimate considering that ~ 4 of the 29 $\Delta_{12} > 0$ cases are upper limits. For the high $L_{14-195\text{keV}}$ sample, where the mean Δ_{12} is positive, 58 cases out of 600 bootstraps give $\Delta_{12} < 0$. Thus the SFR is more enhanced in type 1 than in type 2 sources in the high X-ray luminosity sample with only a marginal significance.</p>
</div>
<div data-bbox="473 904 497 920" data-label="Page-Footer">
12</div>

One important question is whether there is any systematic difference of Δ_{12} values between high and low $L_{14-195\text{keV}}$ samples. In order to test whether the Δ_{12} is significantly different between the high and low $L_{14-195\text{keV}}$ samples, we calculated the difference ($\Delta_{12,\text{High-}L_X} - \Delta_{12,\text{Low-}L_X}$) for 600 randomly selected high X-ray luminosity-low X-ray luminosity pairs from re-drawn samples (see figure 7). The distribution of ($\Delta_{12,\text{High-}L_X} - \Delta_{12,\text{Low-}L_X}$) shows that the probability that it becomes less than zero by chance is only 0.75%.

7. Discussion/Future Plan

Astronomical surveys are often affected by a selection effect derived from a preferential detection of intrinsically bright objects. The luminosities of detected objects found in a flux-limited survey presents a strong distance dependence. Lower luminosity objects at high redshift tend to be censored due to the sensitivity limitations of the instruments. Feigelson & Berg (1983) argued that if censored data is properly treated through the use of survival analysis methods, one can remove the redshift dependence from the luminosity relation. Results from simulations presented in Feigelson & Nelson (1985) tend to support these assertions. Cox’s test for correlation can remove the selection effect and recover the latent relationship between the involved variables. Our regression with the E-M algorithm show significant positive correlation between $\log(L_{14-195\text{keV}}/M_{\text{BH}})$ and $\log(L_{3.3\mu\text{m}}/M_{\text{BH}})$ as well as between $\log(L_{14-195\text{keV}})$ and $\log(L_{3.3\mu\text{m}})$, thus there seem to be real underlying correlation between the AGN and circum-nuclear AGN activities. Another effect that might cause spurious correlations is an aperture effect, where more distant AGNs include more star-formation activities from off-circum-nuclear region such as disks. We estimate the degree of this effect by extracting spectra of our nearby AGNs with apertures that cover the entire galaxy. Typically the PAH luminosity increases by a factor of two, where the increase due to finite point spread function of *AKARI* is $\sim 30\%$, which is estimated from the continuum at $\sim 3.3 \mu\text{m}$ of the QSO 3C 273. Since the correlations extends over ~ 1.5 orders of magnitude in both $\log(L_{3.3\mu\text{m}})$ or $\log(L_{3.3\mu\text{m}}/M_{\text{BH}})$, this aperture effect does not alter our correlation results significantly.

Woo et al. (2012) investigated the connection between starburst and AGN activity by comparing the $3.3 \mu\text{m}$ PAH emission and AGN properties of a more distant sample ($z \sim 0.4$) of moderate-luminosity Seyfert 1s. The $3.3 \mu\text{m}$ feature was detected in 7 of 26 target galaxies. They found no strong correlation between the $3.3\mu\text{m}$ global emission of PAH and AGN luminosity at 5100 \AA . Their sample is enclosed within a fairly narrow range of luminosity and little information can be concluded from these observations. However, by combining with data from literature and assuming a fixed scaling relationship between global emission of $3.3 \mu\text{m}$ PAH and nuclear $3.3 \mu\text{m}$ PAH emission (based on *AKARI*/IRC observations of NGC 7469 performed by Imanishi et al. (2010) and ground-based spectrograph with a narrow slit of $1''.6$ by Imanishi & Wada (2004), respectively), they found a correlation with the luminosity of the AGN on a wider luminosity span, suggesting that star formation and AGN activity could be

closely related in the nuclear region. Their adopted flux ratio between nuclear $L_{3.3\mu\text{m}}$ and the global $L_{3.3\mu\text{m}}$ at $z \sim 0.4$ is 0.04.

As found in Oi et al. (2010), we see no clear difference in the $\langle \log(L_{3.3\mu\text{m}}) \rangle$ between the two types of AGNs for our overall sample. Neither do we find significant difference in the $\langle \log(L_{3.3\mu\text{m}}/M_{\text{BH}}) \rangle$ between type 1 and type 2 AGNs if AGNs in all luminosities are included. However, our regression analysis show that type 1 AGNs exhibit steeper slope in the scatter diagram of $\log(L_{3.3\mu\text{m}})$ plotted as a function of $\log(L_{14-195\text{keV}})$. The same trend has been found for the $\log(L_{3.3\mu\text{m}}/M_{\text{BH}})$ plotted as a function of $\log(L_{14-195\text{keV}}/M_{\text{BH}})$. We find that the mean $\log(L_{3.3\mu\text{m}})$ value is significantly larger in the type 2 AGNs than that of type 1 AGNs, if we limit the sample to lower X-ray luminosity AGNs ($\log(L_{14-149\text{keV}}) \leq 43.64$) while we find no statistically significant difference for the higher luminosity AGNs ($\log(L_{14-149\text{keV}}) > 43.64$). A similar trend has been found in the comparison between $\log(L_{3.3\mu\text{m}}/M_{\text{BH}})$ and $\log(L_{14-195\text{keV}}/M_{\text{BH}})$ with a lower statistical significance. We also find a positive correlation between N_{H} and $\log(L_{3.3\mu\text{m}})$ for the low X-ray luminosity sample only, while no significant correlations have been found between N_{H} and $\log(L_{3.3\mu\text{m}}/M_{\text{BH}})$.

In summary, our analysis found enhanced star-formation for low X-ray luminosity type 2 Seyferts than type 1 Seyferts, while we find no significant difference in high X-ray luminosity AGNs. Thus the Seyfert type dependence of the SFR is luminosity dependent. As seen in Fig. 7, the X-ray luminosity dependence of the AGN type versus SFR relation is statistically robust.

Although it is highly speculative yet, one may interpret this observation as follows. In the low luminosity AGNs, the difference between type 1 and type 2 AGNs may reflect an evolution sequence, where in the early stage of AGN activity, the kpc-scale circum-nuclear star formation, which feeds the central black hole still remains and therefore the AGNs are still surrounded by thick torus, which has a higher chance to be observed as type 2 AGNs. As the starburst fades away which may or may not be quenched by the AGN feedback, the scale height of the torus gets lower and they have more chance to be observed as type 1's. On the other hand, the situation in high luminosity AGNs might be different. It is well known that the type 2 or absorbed AGN fraction (number density of those with $N_{\text{H}} = 10^{22-24}\text{cm}^{-1}$ to that of $N_{\text{H}} < 10^{24}\text{cm}^{-1}$) among X-ray AGNs (excluding highly unexplored population of Compton-thick AGNs with $N_{\text{H}} > 10^{24}\text{cm}^{-1}$) decreases with X-ray luminosity (e.g. Hasinger 2008; Ueda et al. 2014). Thus, on average, the X-ray high luminosity AGNs are surrounded by a thinner torus and it is not unreasonable to assume that the dispersion of the torus opening angles is smaller at high X-ray luminosities than at lower luminosities. Thus at high luminosities, the difference between type 1's and type 2's might be mainly caused by the line-of-sight effect.

An underlying assumption of the survival analysis is that the intrinsic scatter around the best-fit line (regression) or the mean value (two sample tests) is gaussian, which is not guaranteed. Thus it is important to confirm (or deny) our results with as few upper limits as possible.

In our future paper, we will extend our analysis to Spitzer IRS spectroscopy from the archive to utilize the PAH features at $6.2 \mu\text{m}$, $7.7 \mu\text{m}$, $11.3 \mu\text{m}$ and $17 \mu\text{m}$. By involving these PAH lines, we will be able to reduce the number of upper-limits for more robust conclusions.

8. Conclusions

We investigate the $2.5\text{--}5 \mu\text{m}$ spectra of 54 bright nearby non-blazar AGNs from the 9-month *Swift* BAT catalog using *AKARI*/IRC. We investigate the relation between AGN type/absorption and star formation activities. From our present work, we conclude the following:

- We have detected $3.3 \mu\text{m}$ PAH emission from 24 out of 54 flux limited sample of hard X-ray selected AGNs.
- Strong correlations have been found between $\log(L_{14\text{--}195\text{keV}})$ and $\log(L_{3.3\mu\text{m}})$ as well as between $\log(L_{14\text{--}195\text{keV}}/M_{\text{BH}})$ and $\log(L_{3.3\mu\text{m}}/M_{\text{BH}})$ for both optical and X-ray classified type 1 AGNs.
- We have found no statistical difference in the mean circum-nuclear SFR, traced by the PAH $3.3 \mu\text{m}$ emission, between type 1 and type 2 AGNs for our overall sample.
- If we limit ourselves to low luminosity AGNs, we have stronger nuclear starburst activity in type 2 AGNs than type 1 AGNs. There is no significant difference in the star-formation activity between high luminosity type 1 and type 2 AGNs.
- A similar trend has been found for the SSFR, between low and high Eddington ratio samples, although the statistical significance is lower.
- Significant correlation have been found between $\log(N_{\text{H}})$ and $\log(L_{3.3\mu\text{m}})$ for the Low- L_{X} sample, while no significant correlations have been found for the high L_{X} sample. The significance of correlations between $\log(N_{\text{H}})$ and $\log(L_{3.3\mu\text{m}}/M_{\text{BH}})$ in any sample are much weaker, if any.
- Our results suggest that the difference between type 1/type 2 in low luminosity AGNs may reflect an evolution sequence, where more obscuring material is available around low luminosity type 2 AGNs when the circum-nuclear star-formation is feeding the central engine. At high luminosities, the difference between the two types may be mainly from the orientation effect.
- Our analysis depends on the validity of the survival analysis in the presence of upper limits of the $3.3 \mu\text{m}$ luminosities. Our findings have to be confirmed with other measures of the star formation activity that are not contaminated by the AGNs, such as other PAH features measured with *Spitzer* IRS.

This work has been supported by CONACyT Grant 179662 and DGAPA-Universidad

Nacional Autónoma de México (UNAM) Grant PAPIIT IN104113. This work is also supported by the Grant-in-Aid for Scientific Research 23540273 (MI) and 26400228 (YU) from the Ministry of Education, Culture, Sports, Science and Technology of Japan (MEXT). This research is based on observations with *AKARI*, a Japan Aerospace Exploration Agency (JAXA) project with the participation of ESA. The *Swift*/BAT 9-month cataloge site is managed by the NASA Goddard Space Flight Center.

References

- Ajello, M., Alexander, D. M., Greiner, J., Madejski, G. M., Gehrels, N., & Burlon, D. 2012, *ApJ*, 749, 21
- Alexander, D. M., & Hickox, R. C. 2012, *NewAR*, 56, 93
- Allevato, V., Finoguenov, A., Cappelluti, N., Miyaji, T., Hasinger, G., Salvato, M., Brusa, M., Gilli, R., Zamorani, G., Shankar, F., James, J. B., McCracken, H. J., Bongiorno, A., Merloni, A., Peacock, J. A., Silverman, J., & Comastri, A. 2011, *ApJ*, 736, 99
- Antonucci, R. 1993, *ARA&A*, 31, 473
- Brinchmann, J., & Ellis, R. S. 2000, *ApJ*, 536, L77
- Bundy, K., Georgakakis, A., Nandra, K., Ellis, R., Conselice, C., Laird, E., Coil, A., et al. 2008, *ApJ*, 681, 931
- Cappelluti, N., Ajello, M., Burlon, D., Krumpke, M., Miyaji, T., Bonoli, S., & Greiner, J. 2010, *ApJ*, 716, 2843
- Cardelli, J. A., Clayton, G. C., & Mathis, J. S. 1989, *ApJ*, 345, 245 f
- Cid Fernandes, R., Gu, Q., Melnick, J., Terlevich, E., Terlevich, R., Kunth, D., Rodrigues Lacerda, R., & Joguet, B. 2004, *MNRAS*, 355, 273
- Clavel, J., et al. 2000, *A&A*, 357, 839
- Diamond-Stanic, A. & Reike, G. 2012, *ApJ*, 746, 168
- Elitzur, M. 2012, *ApJ*, 747, 33
- Feigelson, E. D., & Berg, C. 1983, *ApJ*, 269, 400
- Feigelson, E. D., Nelson, P. I. 1985, *ApJ*, 293, 192
- Freudling, W., Siebenmorgen, R., & Haas, M. 2003, *ApJ*, 599, L13
- Gaskell, C. M., 1985, *Nature*, 315, 386
- Genzel, R., Lutz, D., Sturm E., Egami E., & Kunze D. 1998, *ApJ*, 498, 579
- Haas, M., Siebenmorgen, R., Schulz, B., Krügel, E., & Chini, R. 2005, *A&A*, 442, 39
- Haiman, Z., & Hui, L. 2001, *ApJ*, 547, 27
- Hasinger, G. 2008, *A&A*, 490, 905
- Hickox, R. C., Myers, A. D., Brodwin, M., Alexander, D. M., Forman, W. R., Jones, C., Murray, S. S., Brown, M. J. I., Cool, R. J., Kochanek, C. S., Dey, A., Jannuzi, B. T., Eisenstein, D., Assef, R. J., Eisenhardt, P. R., Gorjian, V., Stern, D., Le Floch, E., Caldwell, N., Goulding, A. D., & Mullaney, J. R. 2010, *ApJ*, 716, 2843
- Howell, J. H., Mazzarella, J. M., Chan, B. H. P., Lord, S., Surace, J. A, et al. 2007, *ApJ*, 134, 2086
- Ichikawa, K., Ueda, Y., Terashima, Y., Oyabu, S., Gandhi, P., Matsuta, K., & Nakagawa, T. 2012, *ApJ*, 754, 45
- Ichikawa, K., Ueda, Y., Terashima, Y., Oyabu, S., Gandhi, P., Matsuta, K., & Nakagawa, T. 2012, "Torus Workshop Proceedings", p. 109 (Texas:University of Texas at San Antonio)
- Imanishi, M. 2003, *ApJ*, 599, 918
- Imanishi, M. & Dudley, C. C. 2000, *ApJ*, 545, 701
- Imanishi, M., Nakagawa, T., Shirahata, M., Ohyama, Y., & Onaka, T. 2010, *ApJ*, 721, 1233
- Imanishi, M. & Wada, K. 2004, *ApJ*, 617, 214
- Isobe, T., Feigelson, E. D., & Nelson, P. I. 1986, *ApJ*, 306, 490

James, F., & Roos, M. 1975, *ApJ*, 10, 343

Kawakatu, N., & Wada, K. 2008, *ApJ*, 681, 73

Kennicutt, R. C. 1998, *ARA&A*, 36, 189

Krivonos, R., Revnivtsev, M., Tsygankov, S. et al. 2010, *A&A*, 519, 107

La Franca, F., Fiore, F., Comastri, A., et al. 2005, *ApJ*, 635, 864

Lagos, Claudia del P., Cora, S., & Padilla, N. 2008, *ApJ*, 758, 1

LaMassa, S. M., Heckman, T. M., Ptak, A., Schiminovich, D., O’Dowd, M., & Bertincourt, B. 2012, *ApJ*, 758, 1

Lavalley, M. P., Isobe, T., & Feigelson, E. D., 1992, in *Astronomical Data Analysis Software and Systems I*, eds. D. M. Worrall, C. Biemesderfer, & J. Barnes (San Francisco: ASP), 245

Lawrence, A., & Elvis, M. 1982, *ApJ*, 256, 410

Lawrence, A., & Elvis, M. 2010, *ApJ*, 714, 561

Lusso, E., Comastri, A., Simmons, B. D., Mignoli, M., Zamorani, G., Vignali, C., Brusa, M., Shankar, F., Lutz, D., Trump, J. R., et al. 2012, *MNRAS*, 425, 623

Lutz, D., Spoon, H. W. W., Rigopoulou, D., Moorwood, A. F. M., & Genzel, R. 1998, *ApJ*, 505, L103

Maiolino, R., & Rissaliti, G. 2007, *ASPCS*, 373, 447

Martini, P., & Weinberg, D. 2001, *ApJ*, 547, 12

Mihos, C. J., & Hernquist, L. 1994, *ApJ*, 425, L13

Mouri, H., Kawara, K., Taniguchi, Y., & Nishida, M. 1990, *ApJ*, 356, L39

Moorwood, A. F. M. 1986, *ApJ*, 166, 4

Murakami, H., Baba, H., Barthel, P., Clements, D. L., Cohen, M., Doi, Y., Enya, K., Figueredo, E., Fujishiro, N., Fujiwara, H., & Fujiwara, M. 2007, *PASJ*, 59, 369

Mushotzky, R.F., Winter, L.M., McIntosh, D.H., & Tueller, J. 2008, *ApJ*, 684, 65

Nishiyama, S., Nagata, T., Kusakabe, N., Matsunaga, N., Naoi, T., Kato, D., Nagashima, C., Sugitani, K., Tamura, M., Tanabé, T., & Sato, S. 2006, *ApJ*, 638, 839

Nishiyama, S., Tamura, M., Hatano, H., Kato, D., Tanabé, T., Sugitani, K., & Nagata, T. 2009, *ApJ*, 696, 1407

Noguchi, M. 1988, *A&A*, 203, 259

Tueller, J., Baumgartner, W. H., Markwardt, C. B., et al. 2010, *ApJS*, 186, 378

Tueller, J., Mushotzky, R. F., Barthelmy, S., et al. 2008, *ApJ*, 681, 113

Ohsuga, K. & Umemura, M. 2001, *ApJ*, 559, 157

Ohyama, Y., Onaka, T., Matsuhara, H., Wada, T., Kim, W., Fujishiro, N., Uemizu, K., et al. 2007, *PASJ*, 59, 411

Oi, N., Imanishi, M., & Imase, K. 2010, *PASJ*, 62, 1509

Onaka, T., Lorente, R., Ita Y. et al. (2009) “AKARI IRC Data User Manual for Post-Helium (Phase 3) Mission” (Sagamihara:JAXA/ISAS)

Ramos Almeida, C., Levenson, N. A., Alonso-Herrero, A., Asensio Ramos, A., Rodríguez Espinosa, J. M., Pez García, A. M., Packham, C., Mason, R., Radomski, J. T., & Daz-Santos, T. 2011, *ApJ*, 731, 92

Román-Zúñiga, C. G., Lada, C. J., Muench, A., & Alves, J. F. 2007, *ApJ*, 664, 35

- Sanders, D. B., Soifer, B. T., Elias, J. H., Madore, B. F., Matthews, K., Neugebauer, G., & Scoville, N. Z. 1988, *ApJ*, 325, 74
- Schlegel, D., Finkbeiner, D. P., & Davis, M. 1998, *ApJ*, 638, 839
- Shinozaki, K., Miyaji, T., Ishisaki, Y., Ueda, Y., & Ogasaka, Y. 2006, *ApJ*, 131, 2843S
- Simpson, C. 2005, *MNRAS*, 360, 565
- Taniguchi, Y. 1997, *ApJ*, 487, L17
- Tielens, A. G. G. M. 2008, *ARA&A*, 46, 289
- 1997, *ApJ*, 479, L97
- Ueda, Y., Akiyama, M., Hasinger, G., Miyaji, T., & Watson, M. 2014, *ApJ*, 786, 104
- Ueda, Y., Akiyama, M., Ohta, K., & Miyaji, T. 2003, *ApJ*, 598, 886
- Ueda, Y., Eguchi, S., Terashima, Y., Mushotzky, R., Tueller, J., Markwardt, C., Gehrels, N., Hashimoto, Y., & Potter, S. 2007, *ApJ*, 664, L79
- Ueda, Y., Hiroi, K., Isobe, N., Hayashida, M., Eguchi, S., Sugizaki, M., Kawai, N., Tsunemi, H., Mihara, T., Matsuoka, M., Ishikawa, M., et al. 2011, *PASJ*, 63, 937
- Urry, P., & Padovani, P. 1995, *PASP*, 107, 803
- Vasudevan, R. V., Mushotzky, R. F., Winter, L., & Fabian, A. C. 2009, *MNRAS*, 399, 1553
- Voit, G. M. 1992, *ApJ*, 399, 495
- Watabe, Y., Kawakatu, N., & Imanishi, M. 2008, *ApJ*, 677, 895
- Winter, L. M., Lewis, K. T., Koss, M., Veilleux, S., Keeney, B., Mushotzky, R. F. 2010, *ApJ*, 710, 503
- Winter, L. M., Mushotzky, R. F., Reynolds, C. S. & Tueller, J. 2009, *ApJ*, 690, 1322
- Woo, J., Kim, J., Imanishi, M., & Park, D. 2012, *ApJ*, 143, 49

Table 1: *AKARI*/IRC Observation log for hard X-ray selected AGNs

<i>Swift</i> /BAT Name	Counterpart Name	Observation ID	Observation Date
SWIFT J0048.8+3155	NGC 262	1122156-1	2010-01-15
SWIFT J0123.9-5846	Fairall 9	1340445-1,3	2008-12-01,02
SWIFT J0134.1-3625	NGC 612	1120076-1,2,4,5	2008-06-24,26
SWIFT J0138.6-4001	ESO 297-018	1120074-1,2,3,4,5	2008-06-23
SWIFT J0214.6-0049	Mrk 590	1340446-1,2	2009-07-24
SWIFT J0238.2-5213	ESO 198-024	1122056-1,2,3,4,5	2009-12-25
SWIFT J0319.7+4132	NGC 1275	1120056-1	2009-08-21
SWIFT J0426.2-5711	1H 0419-577	1920103-1,2	2009-01-16
SWIFT J0433.0+0521	3C 120	1340447-1,2,3	2009-02-25
SWIFT J0516.2-0009	Ark 120	1340448-1,2,3	2008-09-09
SWIFT J0519.5-3140	ESO 362-G021	1920114-1,2	2009-03-04
SWIFT J0554.8+4625	MCG+08-11-011	1120063-1,2,3	2009-09-21
SWIFT J0601.9-8636	ESO 005-G004	1120073-1,2,3,4,5	2008-09-19,20
SWIFT J0615.8+7101	Mrk 3	1120001-1,2,3	2008-09-23
SWIFT J0623.9-6058	ESO 121-G028	1122044-1,2,3,5	2009-10-18,24
SWIFT J0651.9+7426	Mrk 6	1120064-1,2,3	2008-09-27
SWIFT J0742.5+4948	Mrk 79	1340470-1,2,3	2008-10-10
SWIFT J0902.0+6007	Mrk 18	1122043-1,2,3,4,5	2009-10-20
SWIFT J0920.8-0805	MCG-01-24-012	1122045-1	2009-11-17
SWIFT J0925.0+5218	Mrk 110	1340451-1,2,3	2009-04-25
SWIFT J0945.6-1420	NGC 2992	3750049-1,2,3	2009-11-25,26
SWIFT J0947.6-3057	MCG-05-23-016	1122050-1,2,3	2009-12-03,05
SWIFT J0959.5-2248	NGC 3081	1120082-1,2,3,4,5	2009-06-02
SWIFT J1031.7-3451	NGC 3281	1120075-1,2	2009-06-17
SWIFT J1049.4+2258	Mrk 417	1120083-1,2	2009-05-26
SWIFT J1106.5+7234	NGC 3516	1122032-1,2,3,4	2009-10-25
SWIFT J1139.0-3743	NGC 3783	1340453-1,2,3	2008-07-03
SWIFT J1143.7+7942	UGC 06728	1122054-1,2,4,5	2009-10-15
SWIFT J1203.0+4433	NGC 4051	1340473-1	2009-05-29
SWIFT J1206.2+5243	NGC 4102	1120232-1,1122090-1	2009-05-25,2009-11-27
SWIFT J1210.5+3924	NGC 4151	1122024-1,1340454-1,2,3	2008-06-03,2009-12-05
SWIFT J1225.8+1240	NGC 4388	1120080-1,2,3	2009-06-21
SWIFT J1238.9-2720	ESO 506-G027	1120078-1,2,3,1120079-1,2	2009-01-10,2009-07-11
SWIFT J1239.6-0519	NGC 4593	1340475-1,2	2008-07-02,2009-01-01

Table 1: (Continued.)

SWIFT J1303.8+5345	SBS 1301+540	1122053-1,2,3,4,5	2009-12-04,05
SWIFT J1305.4-4928	NGC 4945	3180009-1	2007-01-27
SWIFT J1322.2-1641	MCG-03-34-064	1120084-1,2,3,4,5	2008-07-17
SWIFT J1338.2+0433	NGC 5252	1120085-1,2,3,4,5	2009-07-12,13
SWIFT J1349.3-3018	IC 4329A	3750054-1,2,3	2010-01-26
SWIFT J1352.8+6917	Mrk 279	1340458-1,2,3	2008-11-14,15,16
SWIFT J1413.2-0312	NGC 5506	1120068,1,2	2008-07-24
SWIFT J1417.9+2507	NGC 5548	1340460-1,2,3	2008-07-13,14
SWIFT J1442.5-1715	NGC 5728	1120086-1,2,3	2009-08-05,06
SWIFT J1535.9+5751	Mrk 290	1340550-1,2,3	2008-06-29,2009-01-01
SWIFT J1628.1+5145	Mrk 1498	1920237-1	2009-07-31
SWIFT J1842.0+7945	3C 390.3	1340466-1,2,3	2008-09-10
SWIFT J1959.4+4044	Cygnus A	1420108-1	2009-05-09
SWIFT J2028.5+2543	MCG+04-48-002	1120077-1,2,1122037-1,2	2009-05-09,2009-11-09
SWIFT J2044.2-1045	Mrk 509	1340467-1,2,3	2009-04-30
SWIFT J2052.0-5704	IC 5063	1122041-3,4,5	2009-10-20,21
SWIFT J2201.9-3152	NGC 7172	1122046-1,2,3	2009-11-13,14
SWIFT J2209.4-4711	NGC 7213	1120069-1,2,3	2008-11-08
SWIFT J2303.3+0852	NGC 7469	1120055-1,3	2008-06-10
SWIFT J2318.4-4223	NGC 7582	1122034-2,3,4	2009-11-23

Table 2: *Swift*/BAT AGNs with *AKARI*/IRC 2.5–5 μm Spectra

<i>Swift</i> Name	R.A.	Dec.	Object Name	Type	z	$\log(L_{14-195\text{keV}})^*$ [ergs^{-1}]	$\log(M_{\text{BH}})$ [M_{\odot}]	$f_{3.3\mu\text{m}}$ [$10^{-14}\text{ergs}^{-1}\text{cm}^{-2}$]	$L_{3.3\mu\text{m}}$ [10^{41}ergs^{-1}]	$N_{\text{H(abs)}}^{\dagger}$ [10^{22}cm^{-2}]
SWIFT J0048.8+3155	12.19	31.95	NGC 262	Sy2.0	0.015	43.84	7.97	<10.62	<0.47	16_{-3}^{+4}
SWIFT J0134.1-3625	23.49	-36.49	NGC 612 $^{\pi}$	Sy2.0	0.029	44.04	8.47	$17.34_{-1.85}^{+1.65}$	$3.07_{-0.33}^{+0.29}$	$129.7_{-8.3}^{+12.9}$
SWIFT J0138.6-4001	24.66	-40.00	ESO 297-018 $^{\pi}$	Sy2.0	0.025	44.03	9.68	$2.73_{-1.20}^{+1.21}$	$0.34_{-0.15}^{+0.15}$	$41.71_{-2.9}^{+4.7}$
SWIFT J0238.2-5213	39.56	-52.20	ESO 198-024	Sy1.0	0.045	44.38	8.36	<1.45	<0.61	0.100
SWIFT J0319.7+4132	49.94	41.51	NGC 1275	Sy2.0	0.017	43.68	8.53	<20.18	<1.22	0.150
SWIFT J0554.8+4625	88.73	46.43	MCG+08-11-011	Sy1.5	0.020	43.96	8.07	<23.87	<1.98	$0.250_{-0.015}^{+0.016}$
SWIFT J0601.9-8636	91.47	-86.60	ESO 005-G004 $^{\pi}$	Sy2.0	0.006	42.59	7.89	$2.86_{-1.42}^{+1.40}$	$0.02_{-0.01}^{+0.01}$	115
SWIFT J0615.8+7101	93.93	71.02	Mrk 3	Sy2.0	0.013	43.81	8.48	$1.75_{-0.41}^{+0.41}$	$0.06_{-0.01}^{+0.01}$	110
SWIFT J0651.9+7426	103.04	74.42	Mrk 6 $^{\pi}$	Sy1.5	0.018	43.78	8.24	<7.27	<0.51	$3.26_{-1.19}^{+1.33}$
SWIFT J0902.0+6007	135.54	60.08	Mrk 18 $^{\pi}$	Sy2.0	0.011	42.93	7.45	$14.11_{-0.97}^{+0.95}$	$0.34_{-0.02}^{+0.02}$	$18.25_{-2.71}^{+3.64}$
SWIFT J0947.6-3057	146.92	-30.94	MCG-05-23-016	Sy2.0	0.008	43.52	7.66	<7.22	<0.10	$1.600_{-0.006}^{+0.005}$
SWIFT J0959.5-2248	149.86	-22.82	NGC 3081 $^{\pi}$	Sy2.0	0.007	43.16	7.96	$3.80_{-1.19}^{+1.17}$	$0.05_{-0.01}^{+0.01}$	$94.2_{-7.2}^{+6.2}$
SWIFT J1031.7-3451	157.95	-34.86	NGC 3281 $^{\pi}$	Sy2.0	0.010	43.36	8.62	<10.07	<0.22	$86.30_{-16.12}^{+16.32}$
SWIFT J1049.4+2258	162.38	22.97	Mrk 417 $^{\pi}$	Sy2.0	0.032	43.97	8.04	<3.44	<0.74	$85.69_{-6.96}^{+12.73}$
SWIFT J1106.5+7234	166.68	72.57	NGC 3516	Sy1.5	0.008	43.34	8.13	<4.85	<0.07	$0.353_{-0.12}^{+0.32}$
SWIFT J1143.7+7942	176.15	79.67	UGC 06728	Sy1.2	0.006	42.44	6.81	<1.15	<0.01	$0.01_{-0.01}^{+0.01}$
SWIFT J1206.2+5243	181.59	52.72	NGC 4102	Sy2.0	0.002	41.66	7.90	$134.66_{-7.28}^{+7.16}$	$0.20_{-0.01}^{+0.01}$	200
SWIFT J1210.5+3924	182.63	39.40	NGC 4151	Sy1.5	0.003	43.18	7.69	$13.00_{-8.72}^{+8.66}$	$0.03_{-0.02}^{+0.02}$	$5.32_{-0.08}^{+0.07}$
SWIFT J1225.8+1240	186.44	12.66	NGC 4388	Sy2.0	0.008	43.74	8.53	$8.14_{-1.88}^{+1.87}$	$0.11_{-0.03}^{+0.03}$	$36.17_{-3.82}^{+3.81}$
SWIFT J1238.9-2720	189.73	-27.30	ESO 506-G027 $^{\pi}$	Sy2.0	0.025	44.29	8.59	$2.81_{-1.09}^{+1.08}$	$0.35_{-0.14}^{+0.14}$	$76.82_{-6.79}^{+7.37}$
SWIFT J1322.2-1641	200.62	-16.74	MCG-03-34-064	Sy1.8	0.016	43.29	8.28	$4.54_{-1.49}^{+1.48}$	$0.24_{-0.08}^{+0.08}$	$40.73_{-4.30}^{+4.79}$
SWIFT J1338.2+0433	204.57	4.54	NGC 5252	Sy1.9	0.022	43.99	8.64	<3.94	<0.41	$4.34_{-0.42}^{+0.52}$
SWIFT J1413.2-0312	213.30	-3.20	NGC 5506	Sy1.9	0.006	43.34	7.77	$15.25_{-5.85}^{+5.81}$	$0.11_{-0.04}^{+0.04}$	$2.78_{-0.05}^{+0.05}$

Table 2: (Continued.)

Swift Name	R.A.	Dec.	Object Name	Type	z	$\log(L_{14-195\text{keV}})^*$ [ergs $^{-1}$]	$\log(M_{\text{BH}})$ [M_{\odot}]	$f_{3.3\mu\text{m}}$ [$10^{-14}\text{ergs}^{-1}\text{cm}^{-2}$]	$L_{3.3\mu\text{m}}$ [10^{41}ergs^{-1}]	$N_{\text{H(abs)}}^{\dagger}$ [10^{22}cm^{-2}]
SWIFT J1442.5-1715	220.60	-17.23	NGC 5728	Sy2.0	0.009	43.31	8.53	$18.95^{+5.41}_{-4.83}$	$0.32^{+0.09}_{-0.08}$	$82.0^{+5.3}_{-5.0}$
SWIFT J1959.4+4044	299.89	40.73	Cygnus A	Sy2.0	0.056	44.96	9.39	<8.03	<5.25	11^{+21}_{-6}
SWIFT J2028.5+2543	307.14	25.73	MCG+04-48-002	Sy2.0	0.013	43.58	7.50	$49.46^{+2.15}_{-2.19}$	$1.87^{+0.08}_{-0.08}$	$96.00^{+51.97}_{-27.77}$
SWIFT J2052.0-5704	313.00	-57.07	IC 5063 $^{\pi}$	Sy2.0	0.011	43.39	7.68	$8.00^{+2.62}_{-2.66}$	$0.20^{+0.07}_{-0.07}$	$21.78^{+2.24}_{-2.06}$
SWIFT J2209.4-4711	332.32	-47.16	NGC 7213	Sy1.5	0.005	42.64	8.63	<6.30	<0.04	$0.025^{+0.011}_{-0.012}$
SWIFT J2303.3+0852	345.81	8.86	NGC 7469	Sy1.2	0.016	43.60	8.64	$79.76^{+6.73}_{-7.11}$	$4.16^{+0.35}_{-0.37}$	0.041
SWIFT J2318.4-4223	349.59	-42.36	NGC 7582	Sy2.0	0.005	42.68	8.31	$84.26^{+6.77}_{-6.62}$	$0.45^{+0.04}_{-0.04}$	33
SWIFT J0623.9-6058	95.98	-60.97	ESO 121-G028	Sy2.0	0.040	44.03	9.00	<0.81	<0.27	$16.19^{+12.6}_{-9.4}$
SWIFT J0920.8-0805	140.21	-8.07	MCG-01-24-012	Sy2.0	0.019	43.60	7.16	<6.59	<0.50	$11.44^{+2.82}_{-2.27}$
SWIFT J1628.1+5145	247.04	51.75	Mrk 1498 $^{\pi}$	Sy1.9	0.054	44.49	8.59	<10.18	<6.32	$17.84^{+2.37}_{-1.82}$
SWIFT J0123.9-5846	20.94	-58.79	Fairall 9	Sy1.2	0.047	44.42	8.91	<3.84	<1.74	0.023
SWIFT J2044.2-1045	33.69	-0.79	Mrk 590	Sy1.0	0.026	43.43	8.87	<4.13	<0.57	0.027
SWIFT J0426.2-5711	66.50	-57.20	1H 0419-577	Sy1.5	0.104	44.77	9.00	<5.63	<13.53	204
SWIFT J0433.0+0521	68.29	5.36	3C 120	Sy1.0	0.033	44.48	8.56	$5.44^{+2.62}_{-2.66}$	$1.19^{+0.57}_{-0.58}$	$0.16^{+0.01}_{-0.01}$
SWIFT J0516.2-0009	79.05	-0.15	Ark 120	Sy1.0	0.032	44.23	8.74	<6.76	<1.45	0.020
SWIFT J0519.5-3140	80.74	-36.45	ESO 362-G021	Sy1.0	0.056	42.27	9.00	<2.63	<1.75	0.010
SWIFT J0742.5+4948	115.60	49.81	Mrk 79	Sy1.2	0.022	43.74	8.42	<7.42	<0.72	0.006
SWIFT J0925.0+5218	141.30	52.28	Mrk 110 ‡	Sy1.0	0.035	44.25	7.80	<6.20	<1.56	$0.02^{+0.01}_{-0.01}$
SWIFT J0945.6-1420	146.44	-14.32	NGC 2992	Sy1.9	0.007	42.80	8.04	$8.88^{+1.75}_{-1.77}$	$0.10^{+0.02}_{-0.02}$	$1.19^{+2.21}_{-0.09}$
SWIFT J1139.0-3743	174.76	-37.74	NGC 3783	Sy1.5	0.009	43.61	8.21	<12.29	<0.23	$0.57^{+0.21}_{-0.14}$
SWIFT J1203.0+4433	180.78	44.52	NGC 4051 ‡	Sy1.5	0.002	41.71	7.27	<18.76	<0.02	0.029
SWIFT J1239.6-0519	189.91	-5.34	NGC 4593	Sy1.0	0.009	43.25	8.61	<9.74	<0.15	$0.031^{+0.011}_{-0.012}$
SWIFT J1303.8+5345	196.02	53.78	SBS 1301+540	Sy1.0	0.029	43.92	7.54	<3.37	<0.60	0.060
SWIFT J1305.4-4928	196.36	-49.46	NGC 4945	Sy2.0	0.001	42.41	6.04	$273.00^{+23.51}_{-24.31}$	$0.18^{+0.02}_{-0.02}$	530

Table 2: (Continued.)

Swift Name	R.A.	Dec.	Object Name	Type	z	$\log(L_{14-195\text{keV}})^*$ [ergs $^{-1}$]	$\log(M_{\text{BH}})$ [M_{\odot}]	$f_{3.3\mu\text{m}}$ [$10^{-14}\text{ergs}^{-1}\text{cm}^{-2}$]	$L_{3.3\mu\text{m}}$ [10^{41}ergs^{-1}]	$N_{\text{H(abs)}}^{\dagger}$ [10^{22}cm^{-2}]
SWIFT J1349.3-3018	207.32	-30.30	IC 4329A	Sy1.2	0.016	44.28	8.52	$16.81^{+5.52}_{-5.54}$	$0.85^{+0.28}_{-0.28}$	$0.61^{+0.03}_{-0.03}$
SWIFT J1352.8+6917	208.26	69.30	Mrk 279	Sy1.5	0.030	44.05	8.62	<5.19	<0.96	0.013
SWIFT J1417.9+2507	214.49	25.13	NGC 5548	Sy1.5	0.017	43.73	8.42	$4.21^{+2.12}_{-2.14}$	$0.24^{+0.12}_{-0.12}$	$0.07^{+0.04}_{-0.05}$
SWIFT J1535.9+5751	233.97	57.87	Mrk 290	Sy1.5	0.029	43.71	7.68	<2.68	<0.47	$0.15^{+0.03}_{-0.05}$
SWIFT J1842.0+7945	280.55	79.77	3C 390.3	Sy1.0	0.056	44.92	8.52	<3.40	<2.22	$0.12^{+0.03}_{-0.03}$
SWIFT J2044.2-1045	311.03	-10.72	Mrk 509	Sy1.5	0.034	44.41	8.59	$8.91^{+2.87}_{-2.89}$	$2.12^{+0.68}_{-0.69}$	$0.015^{+0.008}_{-0.008}$
SWIFT J2201.9-3152	330.51	-31.86	NGC 7172	Sy2.0	0.008	43.48	8.31	$26.59^{+3.92}_{-3.96}$	$0.39^{+0.06}_{-0.06}$	$8.19^{+3.42}_{-3.30}$

* X-ray luminosity in the 14–195 keV band (ergs $^{-1}$).

\dagger N_{H} value taken from Winter et al. (2009) and Ichikawa et al. (2012a) and references there in.

π Classified as “New Type” object. See Ueda et al. (2007)

\ddagger Narrow Line Seyfert 1 (NLS1) object.

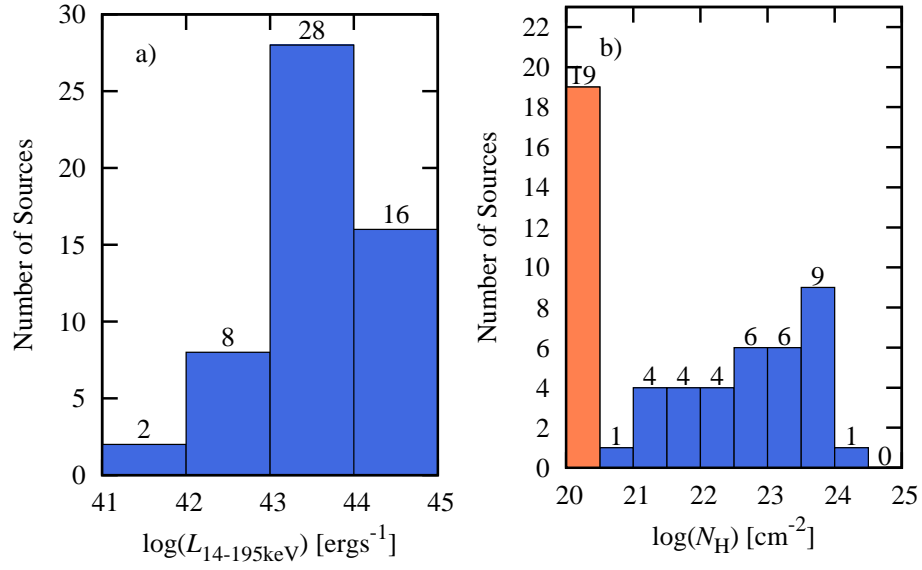


Fig. 1: (a) Distribution of the $\log(L_{14-195\text{keV}})$ of the sample. (b) Distribution of the absorbing column density (N_{H} in units of cm^{-2}) obtained from softer X-ray ($E < 10$ keV) spectra of our sample (Winter et al. 2009; Ichikawa et al. 2012a). (Color figures are available on the electronic version only.)

Table 3: Linear regression parameters obtained using the E-M method under ASURV.

$\log(L_{3.3\mu\text{m}}) = a_0 \{ \log(L_{14-195\text{keV}}) - c_0 \} + b_0$						
Sample	No.	Up.*	a_0	b_0	$\langle \log(L_{3.3\mu\text{m}}) \rangle$	P [†]
All AGNs	54	30	0.42±0.14	40.20±0.11	40.07±0.12	0.01
Optical type 1	26	20	1.05±0.27	39.92±0.24	39.68±0.22	0.02
Optical type 2	28	10	0.11±0.17	40.27±0.12	40.23±0.11	0.66
X-ray type 1	24	19	1.11±0.35	39.83±0.33	39.61±0.24	0.05
X-ray type 2	30	11	0.12±0.18	40.23±0.12	40.19±0.11	0.56
$\log(L_{3.3\mu\text{m}}/M_{\text{BH}}) = a_1 \{ \log(L_{14-195\text{keV}}/M_{\text{BH}}) - c_1 \} + b_1$						
Sample	No.	Up.	a_1	b_1	$\langle \log(L_{3.3\mu\text{m}}/M_{\text{BH}}) \rangle$	P
All AGNs	54	30	0.73±0.17	31.97±0.13	31.88±0.13	0.002
Optical type 1	26	20	1.56±0.37	31.55±0.26	31.62±0.21	0.005
Optical type 2	28	10	0.62±0.23	32.16±0.16	32.01±0.16	0.10
X-ray type 1	24	19	1.59±0.43	31.48±0.33	31.53±0.21	0.006
X-ray type 2	30	11	0.58±0.22	32.13±0.15	32.00±0.15	0.10
$\log(L_{3.3\mu\text{m}}) = a_2 \{ \log(N_H) - c_2 \} + b_2$						
Sample	No.	Up.	a_2	b_2	$\langle \log(L_{3.3\mu\text{m}}) \rangle$	P
All	54	30	0.14±0.09	40.02±0.14	40.07±0.12	0.003
$\log(L_{14-195\text{keV}}) \leq 43.64$	26	11	0.28±0.13	39.78±0.19	39.95±0.15	0.01
$\log(L_{14-195\text{keV}}) > 43.64$	28	19	-0.03±0.09	40.39±0.15	40.37±0.13	0.58
$\log(L_{3.3\mu\text{m}}/M_{\text{BH}}) = a_3 \{ \log(N_H) - c_3 \} + b_3$						
Sample	No.	Up.	a_3	b_3	$\langle \log(L_{3.3\mu\text{m}}/M_{\text{BH}}) \rangle$	P
All	54	30	0.22±0.12	31.71±0.19	31.88±0.13	0.075
$\log(L_{14-195\text{keV}}/M_{\text{BH}}) \leq 35.43$	25	13	0.15±0.10	31.44±0.15	31.52±0.12	0.12
$\log(L_{14-195\text{keV}}/M_{\text{BH}}) > 35.43$	29	17	0.20±0.14	32.23±0.23	32.42±0.14	0.17

* Number of upper-limits in the subsample.

† Correlation probability by Cox's proportional hazard model.

Table 4: Two sample tests for optically and X-ray classified AGNs.

Class.	Criteria	No.	n_1^*	n_2^\dagger	$\langle \log(L_{3.3\mu\text{m}}/M_{\text{BH}}) \rangle$		Gehan's Prob.	logrank Prob.	Peto&Peto Prob.
					Type 1	Type 2			
Optical	All AGNs	54	26	28	31.62±0.21	32.01±0.16	0.27	0.17	0.21
	$\log(L_X/M_{\text{BH}}) \leq 35.43$	25	10	15	31.17±0.15	31.66±0.13	0.14	0.09	0.12
	$\log(L_X/M_{\text{BH}}) > 35.43$	29	16	13	32.21±0.19	32.62±0.20	0.21	0.18	0.18
X-ray	All AGNs	54	24	30	31.53±0.21	32.00±0.15	0.34	0.14	0.20

Class.	Criteria	No.	n_1	n_2	$\langle \log(L_{3.3\mu\text{m}}) \rangle$		Gehan's Prob.	logrank Prob.	Peto&Peto Prob.
					Type 1	Type 2			
Optical	All AGNs	54	26	28	39.68±0.22	40.23±0.11	0.58	0.05	0.22
	$\log(L_X) \leq 43.64$	26	9	17	39.44±0.28	40.19±0.13	0.04	0.02	0.02
	$\log(L_X) > 43.64$	28	17	11	40.59±0.09	40.29±0.19	0.66	0.34	0.50
X-ray	All AGNs	54	24	30	39.61±0.24	40.19±0.11	0.80	0.08	0.37

* Number of type 1 objects contained in the sample.

† Number of type 2 objects contained in the sample.

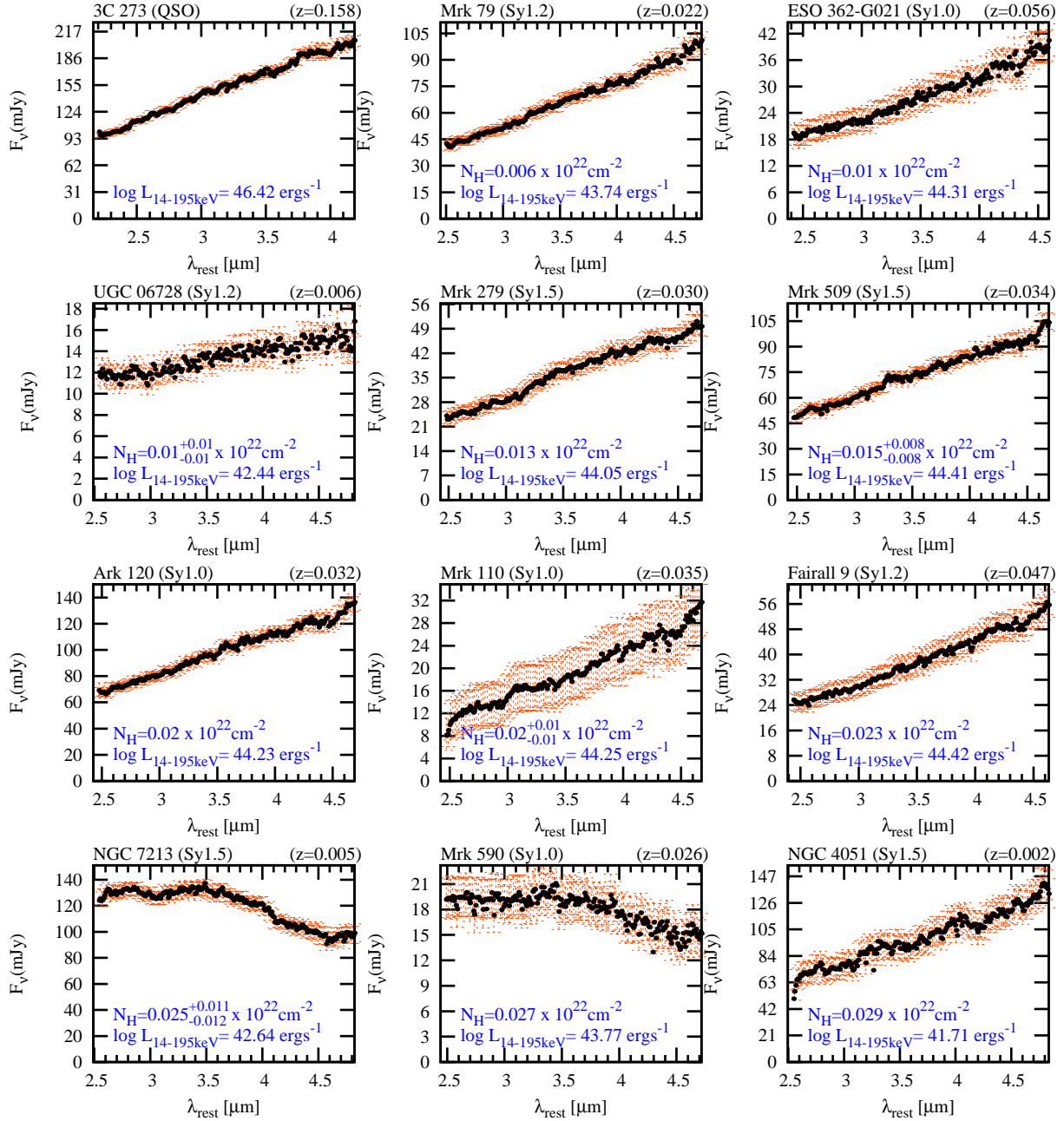


Fig. 2: *AKARI*/*IRC* infrared 2.5–5 μm spectra of our X-ray selected AGN sample. The abscissa is the rest-frame wavelength and the ordinate is the flux F_ν in mJy. Each object shows its name, redshift and N_{H} column density values. X-ray luminosities (in units of ergs^{-1}) in the band 14–195 keV ($L_{14-195\text{keV}}$) were obtained from Tueller et al. (2008). (Color figures are available on the electronic version only.)

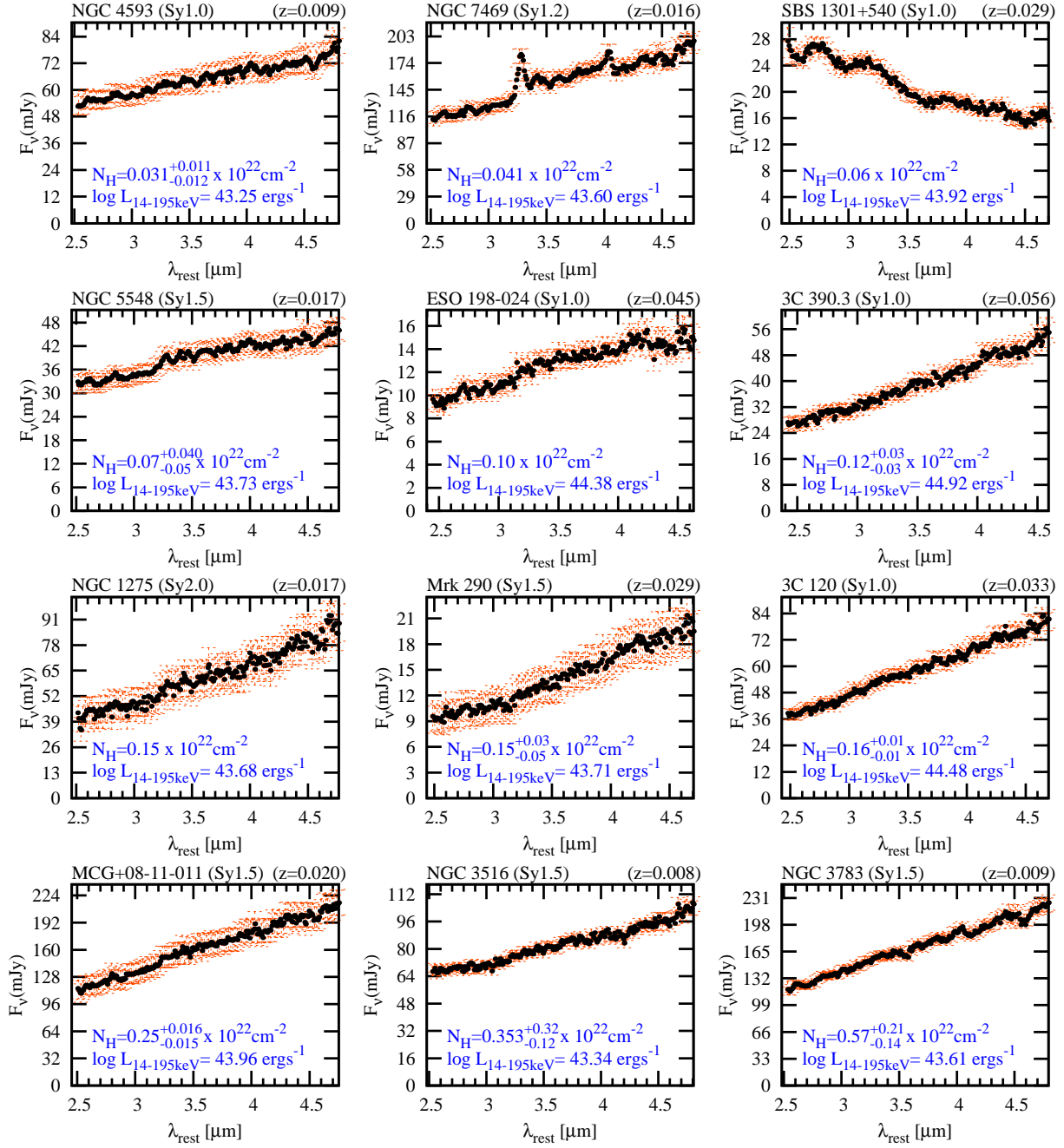


Fig. 2: Continued.

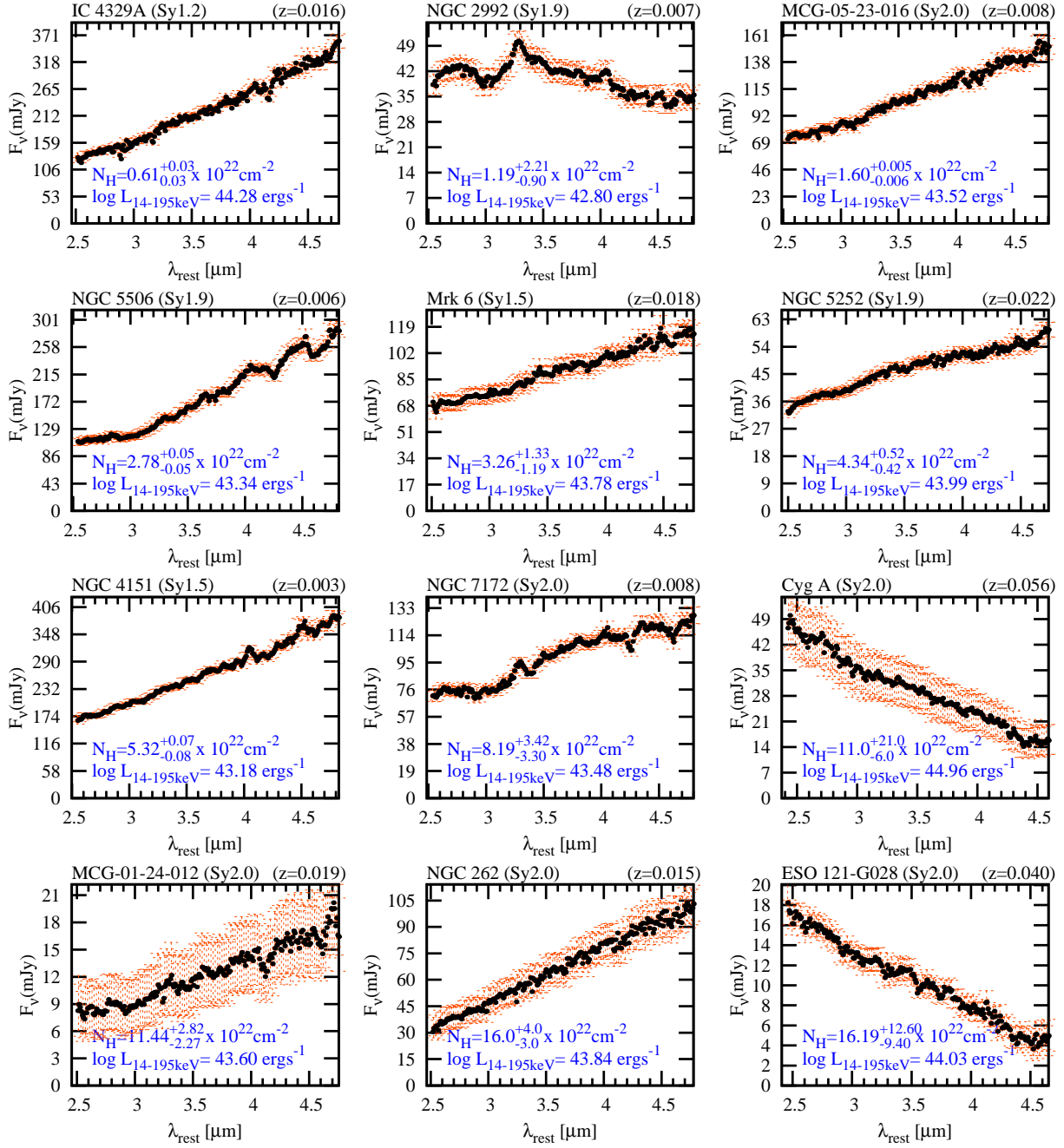


Fig. 2: Continued.

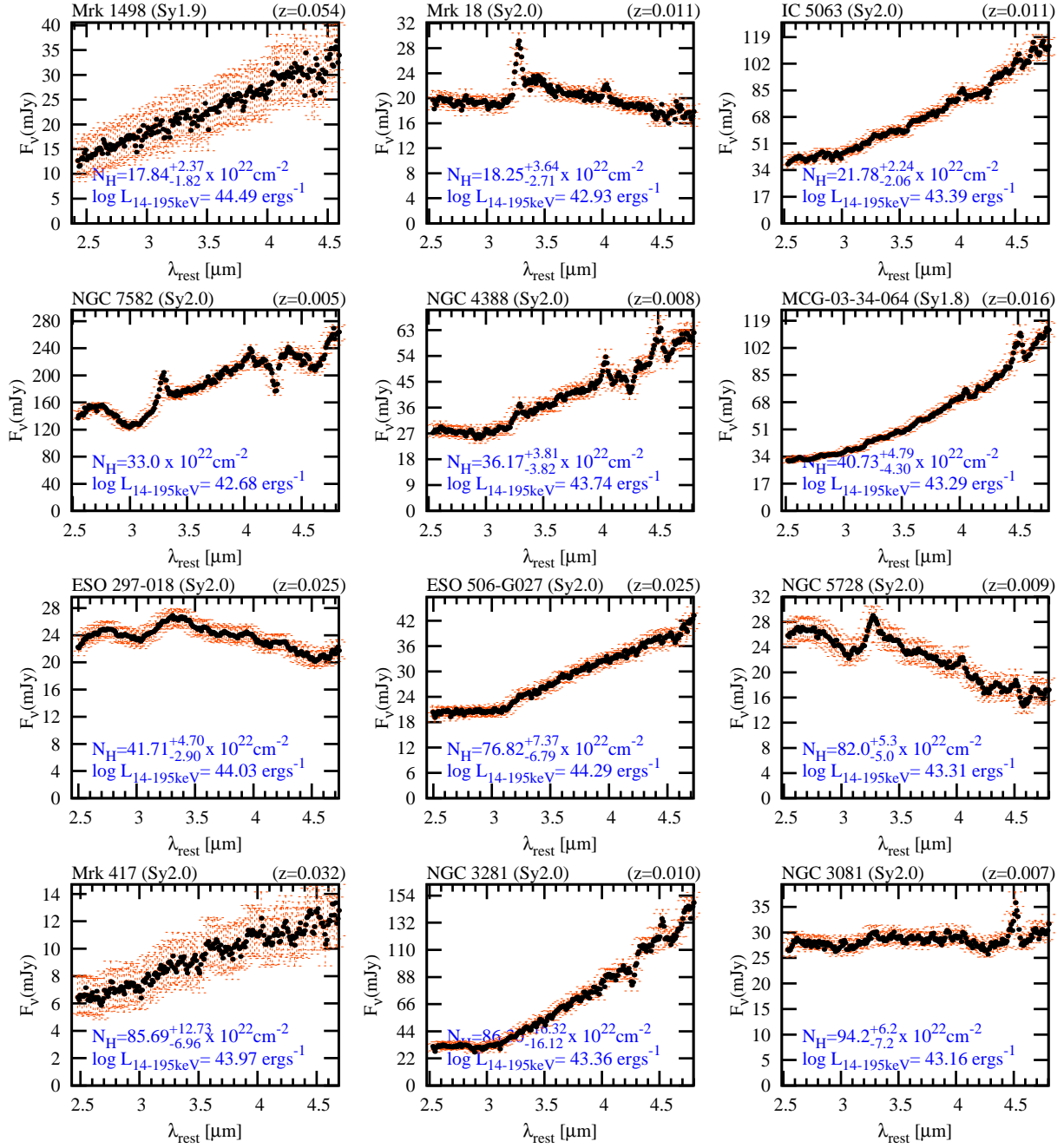


Fig. 2: Continued.

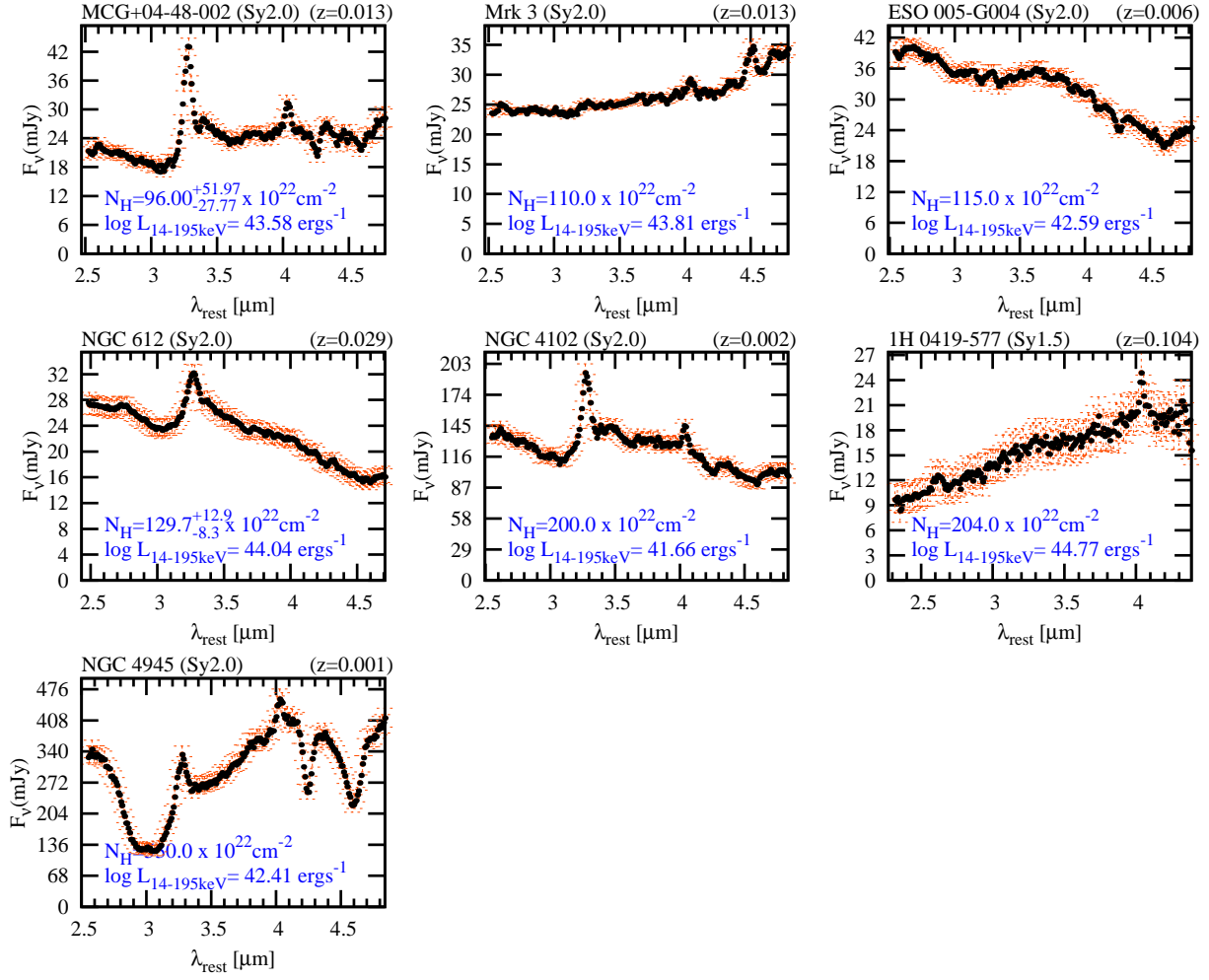


Fig. 2: Continued.

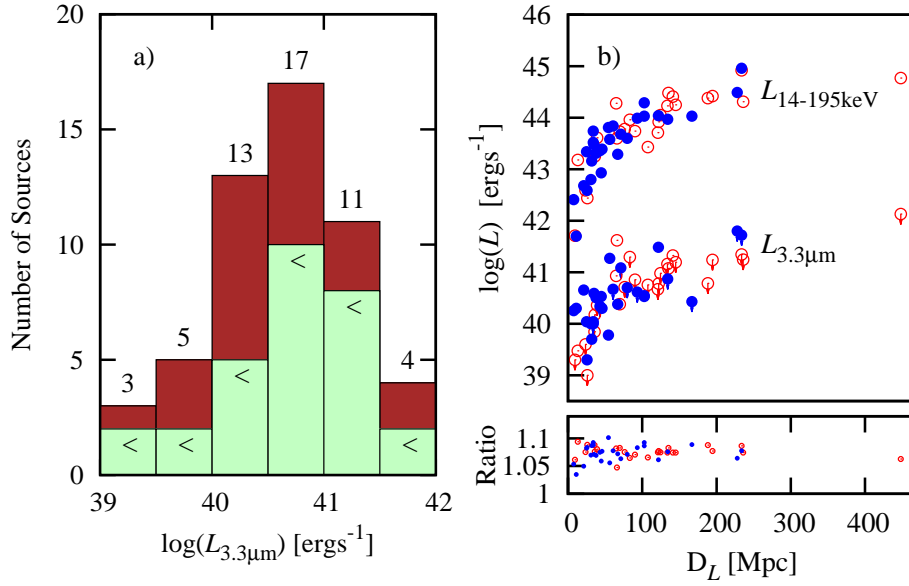


Fig. 3: (a) Distribution of $\log(L_{3.3\mu\text{m}})$ and (b) luminosity-distance relationship of the entire sample: Logarithm of the luminosity of the $3.3 \mu\text{m}$ PAH emission in units of ergs^{-1} (down) and logarithm of the hard-X ray luminosity in the 14 – 195 keV band in units of ergs^{-1} (up). The brown part shows actual detections and the pale green part (with “<” symbols) show upper limits. Open red circles are optically classified Seyfert 1 and solid blue circles are Syeyfert 2s. Small downward arrows are upper-limits. (Color figures are available on the electronic version only.)

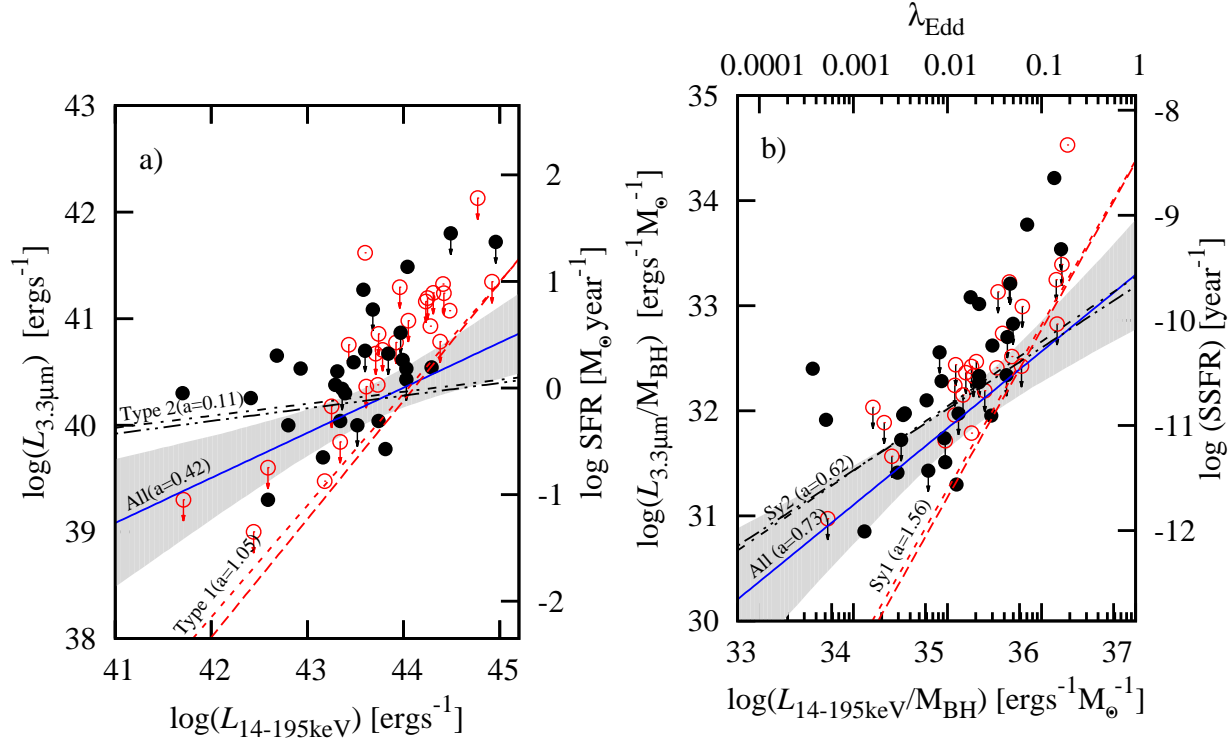


Fig. 4: (a) $\log(L_{14-195\text{keV}})$ versus $\log(L_{3.3\mu\text{m}})$ and (b) $\log(L_{14-195\text{keV}}/M_{\text{BH}})$ versus $\log(L_{3.3\mu\text{m}}/M_{\text{BH}})$ relations. On the right vertical axis of panel (a), approximate star-formation rate corresponding to $\log(L_{3.3\mu\text{m}})$ are shown. Also on the upper horizontal and right vertical axes of panel (b), approximate Eddington ratios, λ_{Edd} , corresponding to the $\log(L_{14-195\text{keV}}/M_{\text{BH}})$ values and the specific star formation rate (SSFR) corresponding to $\log(L_{3.3\mu\text{m}}/M_{\text{BH}})$ are shown respectively. Arrows are for upper-limits. In each figure, the best-fit linear regression for all-AGN sample is shown in solid blue lines, while the error region is shown in gray shades. Open red circles are used for optical type 1 objects and filled black circles for optical type 2 objects. Red dashed and long-dashed lines corresponds to the regression lines for optical and X-ray type 1 objects, respectively. While the black dot-dashed and dot-dot-dashed lines corresponds to the regression lines for optical and X-ray type 2 AGNs, respectively. (Color figures are available on the electronic version only.)

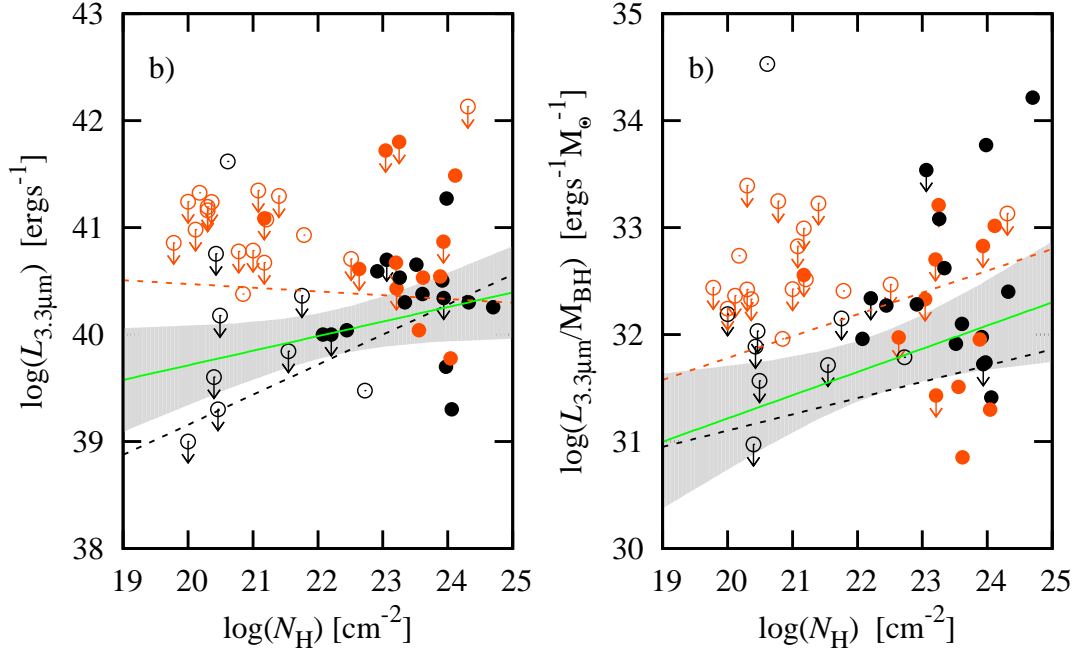


Fig. 5: (a) $\log(L_{3.3\mu\text{m}})$ versus N_{H} relationship. Orange (paler) symbols have been used for AGNs with $\log(L_{14-195\text{keV}}) > 43.64$ and black for $\log(L_{14-195\text{keV}}) \leq 43.64$, orange and black dashed lines are the regression fits for the subsamples, respectively. (b) $\log(L_{3.3\mu\text{m}}/M_{\text{BH}})$ versus N_{H} relationship. Orange symbols have been used for AGN with $\log(L_{3.3\mu\text{m}}/M_{\text{BH}}) > 35.43$ and black for $\log(L_{3.3\mu\text{m}}/M_{\text{BH}}) \leq 35.43$, orange and black dashed lines are the regression fits for the subsamples, respectively. Open circles are for X-ray type 1 objects and filled circles for X-ray type 2 objects. Arrows are for upper-limits. Solid green lines are the linear fits for the whole sample in each case. For numerical details see table 3. (Color figures are available on the electronic version only.)

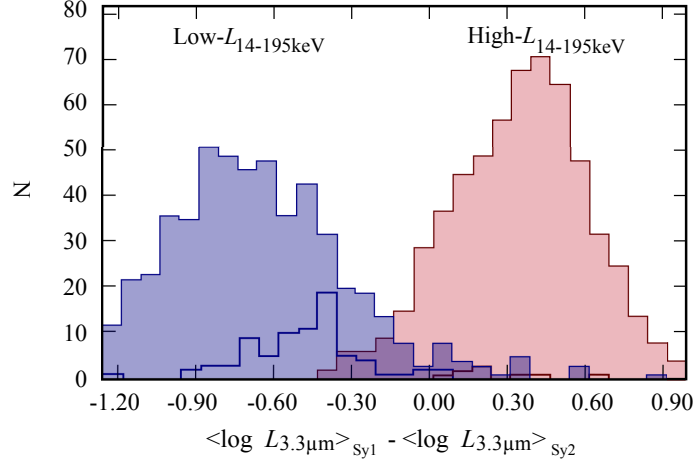


Fig. 6: The bootstrap histograms of $\Delta_{12} = \langle \log L_{3.3\mu\text{m}} \rangle_{\text{Sy1}} - \langle \log L_{3.3\mu\text{m}} \rangle_{\text{Sy2}}$ are shown for the high $L_{14-195\text{keV}}$ (blue/darker histogram) and low $L_{14-195\text{keV}}$ (red/paler histogram) samples. The histograms below thick solid lines, which are labeled as a number of " < " 's show the cases where the TWOST routine fails to give $\langle \log L_{3.3\mu\text{m}} \rangle_{\text{Sy1}}$ due to too many upper limits in the corresponding redrawn sample, in which the upper limits are used for the mean calculations. (Color figures are available on the electronic version only.)

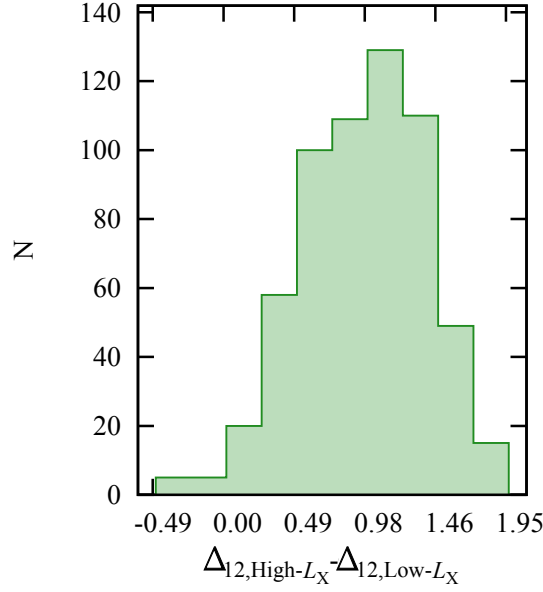


Fig. 7: Histogram of the difference $(\Delta_{12,\text{High-}L_X} - \Delta_{12,\text{Low-}L_X})$ for 600 randomly selected high $L_{14-195\text{keV}}$ and low $L_{14-195\text{keV}}$ pairs from re-drawn samples, respectively. The distribution of $(\Delta_{12,\text{High-}L_X} - \Delta_{12,\text{Low-}L_X})$ shows that the probability that it becomes less than zero by chance is only 0.75%. (Color figures are available on the electronic version only.)